Article

Single-shot parity readout of a minimal Kitaev chain

https://doi.org/10.1038/s41586-025-09927-7

Received: 2 July 2025

Accepted: 17 November 2025

Published online: 11 February 2026

Check for updates

Nick van Loo[1,2,5]✉, Francesco Zatelli[1,2,5], Gorm O. Steffensen[3,5], Bart Roovers[1,2,5], Guanzhong Wang[1,2], Thomas Van Caekenberghe[1,2], Alberto Bordin[1,2], David van Driel[1,2], Yining Zhang[1,2], Wietze D. Huisman[1,2], Ghada Badawy[4], Erik P. A. M. Bakkers[4], Grzegorz P. Mazur[1,2], Ramón Aguado[3] & Leo P. Kouwenhoven[1,2]✉

Protecting qubits from noise is essential for building reliable quantum computers. Topological qubits offer a route to this goal by encoding quantum information non-locally, using pairs of Majorana zero modes. These modes form a shared fermionic state whose occupation—either even or odd—defines the fermionic parity that encodes the qubit[1]. Notably, this parity can only be accessed by a measurement that couples two Majoranas to each other. A promising platform for realizing such qubits is the Kitaev chain[1], implemented in quantum dots coupled using superconductors[2]. Even the minimal two-site chain hosts a pair of Majorana modes, often called ‘poor man’s Majoranas’, which are spatially separated but offer limited protection compared with longer chains[3–5]. Here we introduce a measurement technique that reads out their parity through quantum capacitance. Our method couples two Majoranas and resolves their parity in real time, visible as random telegraph switching with lifetimes exceeding a millisecond. Simultaneous charge sensing confirms that the two parity states are charge neutral and remain indistinguishable to a probe that does not couple the modes. These results establish the essential readout step for time-domain control of Majorana qubits, resolving a long-standing experimental challenge.

In the quest for fault-tolerant quantum computing, Majorana zero modes offer an attractive platform for encoding topological qubits. These qubits, defined by the fermionic parity of spatially separated pairs of Majorana modes, exhibit intrinsic protection against decoherence[1,6–8]. The simplest model supporting these modes is the Kitaev chain: a one-dimensional array of spinless fermions with superconducting pairing[1]. Their recent realization in quantum dots (QDs) coupled using superconductors has opened an exciting new frontier[4,5]. Even the minimal version of these chains hosts a pair of Majorana zero modes at a fine-tuned sweet spot that are often referred to as poor man’s Majoranas (PMMs)[2,3]. At that sweet spot, the even and odd parity states of the chain are degenerate, supporting Majorana modes γ_1 and γ_2 that localize on different QDs. Their spatial separation provides protection against detuning of either dot. However, this protection is fragile: the parity degeneracy splits linearly when perturbing the coupling between the dots, whereas simultaneous detuning of both QDs lifts it quadratically[3]. In longer chains, by contrast, the residual splitting from noise or imperfect tuning decreases exponentially with chain length, which is the defining feature of topological protection[2]. Despite their limited robustness, PMMs are expected to exhibit non-Abelian exchange statistics[9–12].

In general, two Majorana modes form a fermion $c = (\gamma_1 + i\gamma_2)/\sqrt{2}$ whose occupation $P_{12} = i\gamma_1\gamma_2$ stores the quantum information[11,13–15]. Accessing this parity requires coupling the modes to an observable of a detector M_{detector} (for example, the photonic mode of a resonator), introducing an interaction of the form $i\gamma_1\gamma_2M_{\mathrm{detector}}$, as schematically depicted in Fig. 1a,b. This controlled coupling hybridizes the modes and fuses them into an ordinary fermionic level[16]. Parity readout then reduces to measuring the occupation of a fermion in a semiconductor–superconductor hybrid system. Such measurements have been extensively explored using charge sensing[17], dispersive gate sensing[18,19] and circuit quantum electrodynamics[20–22]. Recently, single-shot readout was demonstrated in an interferometry-based implementation exhibiting $h/2e$-periodic bimodality and millisecond-scale lifetimes[23]. The same approach was used in a multi-wire geometry to extract loop-specific parity-switching times[24].

Beyond readout, a central challenge is to preserve parity over time. In practice, conservation of parity can be broken by quasiparticles entering the device, a process known as quasiparticle poisoning. This causes a Majorana qubit to leak out of the computational subspace, destroying the stored quantum information[25]. Similar poisoning limits the performance of superconducting and hybrid qubits[20,26,27]. Characterizing parity lifetimes and achieving high-fidelity parity readout therefore remain critical benchmarks towards Majorana-based qubits and topological quantum computing[23,25,28].

In this work, we introduce a measurement technique that distinguishes the fermionic parity of a minimal Kitaev chain through its

[1]QuTech, Delft University of Technology, Delft, The Netherlands. [2]Kavli Institute of Nanoscience, Delft University of Technology, Delft, The Netherlands. [3]Instituto de Ciencia de Materiales de Madrid (ICMM), Consejo Superior de Investigaciones Científicas (CSIC), Madrid, Spain. [4]Department of Applied Physics, Eindhoven University of Technology, Eindhoven, The Netherlands. [5]These authors contributed equally: Nick van Loo, Francesco Zatelli, Gorm O. Steffensen, Bart Roovers. ✉e-mail: n.vanloo@tudelft.nl; l.p.kouwenhoven@tudelft.nl

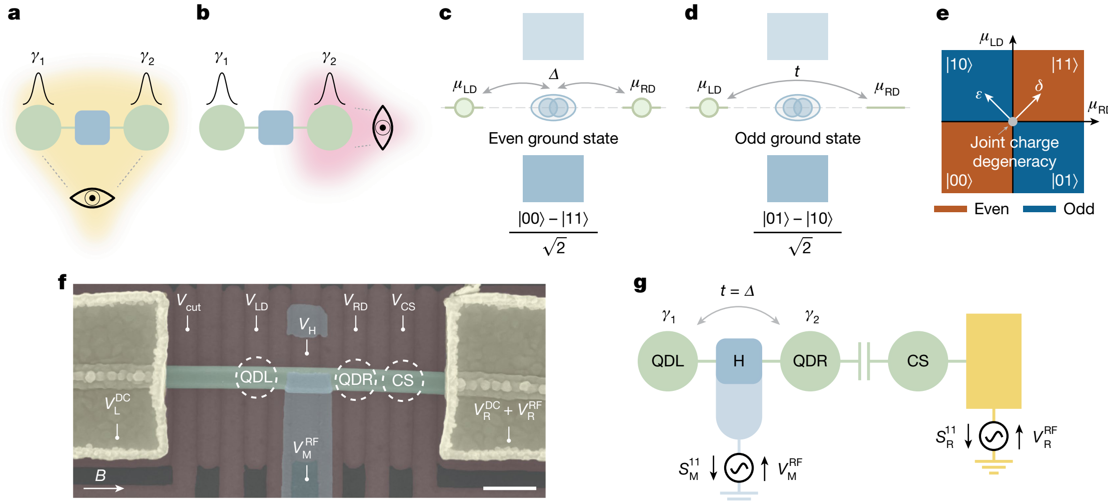

Fig. 1 | Minimal Kitaev chain and parity measurement set-up. **a**, Illustration of two Majorana modes γ_1 and γ_2 on separate dots. A probe acting on both couples them and reveals their parity. **b**, Illustration of a probe acting on only one Majorana without inducing a coupling, so that parity remains indistinguishable. **c**, Energy diagram of two QDs with chemical potentials μ_{LD} and μ_{RD} in the even parity sector, in which $|00\rangle$ and $|11\rangle$ hybridize by means of CAR in the superconductor with amplitude Δ. **d**, Energy diagram of the odd parity sector, in which $|10\rangle$ and $|01\rangle$ hybridize by means of ECT with amplitude t. **e**, Charge-stability diagram of two QDs, showing the detuning axis ε and common-mode axis δ. Orange and blue sectors denote the even and odd parity ground states, respectively. The centre marks the joint charge degeneracy, which is the PMM sweet spot when $t = \Delta$. **f**, False-coloured scanning electron micrograph of the device. The InSb nanowire (green) is proximitized by an Al strip (blue) and contacted by Cr/Au leads (yellow). QDs (QDL, QDR and CS, dashed circles) are defined using Ti/Pd bottom gates (red). The Kitaev chain is tuned by V_{LD}, V_{RD} and V_H. The device is isolated from the left lead using V_{cut}. The CS is controlled with V_{CS} and the nanowire is depleted between QDR and CS. DC (V_L^{DC} and V_R^{DC}) and RF (V_M^{RF} and V_R^{RF}) voltages are applied to the three leads for biasing and reflectometry. A parallel magnetic field $B = 150$ mT ensures spin polarization of the QDs. Scale bar, 200 nm. **g**, Schematic of the readout set-up. The two QDs are coupled through a superconducting segment connected to a RF resonator, for readout by S_M^{11}. Likewise, the CS is read out by a second resonator, S_R^{11}.

quantum capacitance, by detuning the PMMs around the sweet spot and thereby inducing a parity-dependent splitting[9,29]. Unlike earlier dispersive sensing of charge states in QDs and hybrid systems[30–32], our method detects the response directly through the superconducting lead. This reflects the common-mode motion of charge between the dots and the superconductor, providing a new route to dispersive readout that resolves the parity of the chain in real time. By comparing with simultaneous charge sensing of one QD, we further demonstrate that the detected parity states are charge neutral.

Minimal Kitaev chain quantum capacitance

A minimal Kitaev chain consists of two spinless fermionic sites with on-site energies μ_{LD} and μ_{RD}. The sites are coupled by elastic co-tunnelling (ECT) and crossed Andreev reflection (CAR), with amplitudes t and Δ, respectively. Each site can be either occupied or empty, leading to four charge configurations $|n_{LD}n_{RD}\rangle$, in which $n_{LD}, n_{RD} \in \{0, 1\}$. At charge degeneracy, the even states $|00\rangle$ and $|11\rangle$ hybridize by CAR to form bonding and antibonding combinations $|e\rangle = (|00\rangle \pm |11\rangle)/\sqrt{2}$ (Fig. 1c). Likewise, the odd states $|10\rangle$ and $|01\rangle$ hybridize by ECT to form $|o\rangle = (|10\rangle \pm |01\rangle)/\sqrt{2}$ (Fig. 1d). These define two parity branches with distinct energy dispersions:

$$E_e^{\pm} = -\delta \pm \sqrt{\delta^2 + \Delta^2}, \quad (1)$$

$$E_o^{\pm} = -\delta \pm \sqrt{\varepsilon^2 + t^2}. \quad (2)$$

Here $E_e^{\pm}$ and $E_o^{\pm}$ are the even and odd eigenenergies with ± denoting ground and excited states, $\varepsilon = (\mu_{LD} - \mu_{RD})/2$ defines the detuning axis and $\delta = (\mu_{LD} + \mu_{RD})/2$ is the common-mode axis. When $t = \Delta$ and $\mu_{LD} = \mu_{RD} = 0$, the two ground states become degenerate, leading to zero-energy excitations with Majorana character on each dot[3]. The corresponding charge-stability diagram is shown in Fig. 1e, in which the PMM sweet spot is located at the joint charge degeneracy.

Our realization (Fig. 1f) consists of two gate-defined QDs (QDL and QDR) that form a minimal Kitaev chain in an InSb–Al hybrid nanowire[33], with a third dot acting as a nearby charge sensor (CS)[34–36]. Although transport measurements are typically used to set up the Kitaev chain[4], maintaining the required coupling to normal leads during readout would continuously inject quasiparticles that flip the fermion parity. To preserve parity, we instead isolate the device by depleting the nanowire with V_{cut}. The isolated system is then examined through the reflected signal of two multiplexed RF resonators (Fig. 1g): S_M^{11} from the superconducting lead, sensitive to the parity of the chain through quantum capacitance, and S_R^{11} from the nearby CS that monitors local charge. We analyse these signals projected along their principal axes as ΔS_R^{11} and ΔS_M^{11}. Full fabrication and wiring details are given in Methods.

We first focus on the superconducting lead. The applied RF signal induces small oscillations in its electrochemical potential relative to the QDs, effectively modulating the system along the common-mode axis δ. Such oscillations could also weakly shift the energies of Andreev bound states (ABS) and thereby affect the effective couplings, but this effect is negligible owing to strong capacitive coupling between the ABSs and the superconductor. As seen from equations (1) and (2), this reveals a key difference between the parity branches: even states disperse nonlinearly because of hybridization by CAR, whereas the odd states change linearly (Fig. 2a). This is reflected in the curvature of their energy levels and thus in their quantum capacitance, which is proportional to the second derivative of energy with respect to chemical potential (see Methods). Intuitively, the RF oscillation periodically shifts the balance between $|00\rangle$ and $|11\rangle$, inducing charge motion between the QDs and the superconductor and producing a measurable quantum capacitance. By contrast, the odd states $|01\rangle$ and $|10\rangle$ are connected by tunnelling that does not involve net charge transfer to or from the superconductor, yielding zero quantum capacitance. This behaviour appears

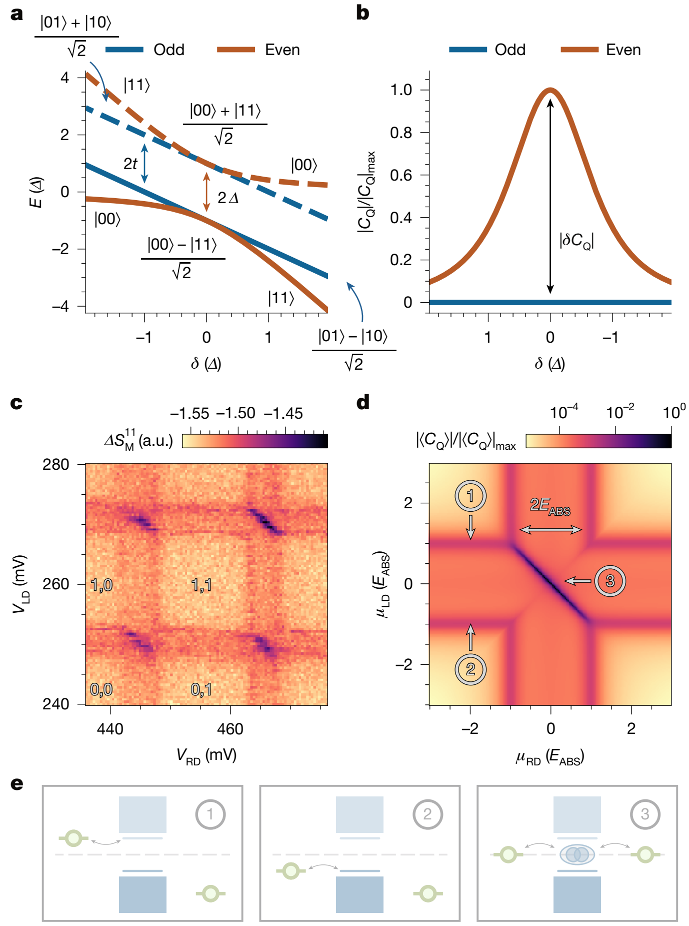

Fig. 2 | Quantum capacitance of the chain. a, Energy dispersion of the even (CAR-coupled) and odd (ECT-coupled) parity states at zero detuning ($\varepsilon = 0$), plotted as a function of the common-mode potential δ along which V^{RF}_M is applied. **b**, Calculated quantum capacitance C_Q for each parity branch, given by the second derivative of energy with respect to chemical potential. A strong contrast δC_Q appears near the degeneracy point at which even states show maximal curvature. **c**, Charge-stability diagram with labelled charge states measured by means of the quantum capacitance signal ΔS^{11}_M in arbitrary units (a.u.). The dominant anti-diagonal lines correspond to $\mu_{LD} = -\mu_{RD}$, at which the strength of CAR is maximal. **d**, Simulation of the quantum capacitance around one charge degeneracy (see Methods), showing features consistent with the experiment. **e**, Energy diagrams of the relevant hybridization processes. (1) and (2) correspond to hybridization between a single dot and the lowest-energy state in the hybrid segment and (3) shows interdot hybridization at joint charge degeneracy.

in Fig. 2b, in which only the even state has a finite signal near $\delta = 0$. Also, the contrast between even and odd parity states reaches a maximum at this point, which scales as $\delta C_Q \propto \Delta^{-1}$ (ref. 9). The resulting parity-dependent frequency shift of the resonator is detected in ΔS^{11}_M, providing a superconducting analogue to reflectometry-based sensing in conventional double dots[32]. In our case, the signal arises from Cooper-pair splitting rather than interdot tunnelling.

Figure 2c shows a measurement of ΔS^{11}_M as the chemical potentials of the two QDs are varied, with weak interdot coupling. The most prominent feature is a strong anti-diagonal line through the joint charge degeneracies, in which |00⟩ and |11⟩ form an equal superposition and the total charge is most susceptible to variations of δ. This results in a pronounced signal that we attribute to quantum capacitance, in agreement with Fig. 2b. Further horizontal and vertical bands appear when only one QD is near resonance. These arise from hybridization between a single dot level and the lowest-energy state in the hybrid segment, generating finite quantum capacitance without interdot coupling. Their widths reflect the energy of this state E_{ABS}, with maximum signal at resonance. Our theoretical model (Fig. 2d; see Methods) qualitatively reproduces these features, treating the hybrid segment as a spinful resonant level coupled to a superconductor in the presence of spin–orbit coupling. The energy diagrams in Fig. 2e illustrate the processes behind the observed signals. The band visibility depends on QD–hybrid coupling strength, whereas the joint resonance signal reflects interdot coupling. Extended Data Fig. 3 shows how tuning the hybrid electrochemical potential through V_H modifies this behaviour. These features help identify suitable joint degeneracies for time-domain parity readout, as discussed next.

Time-resolved parity measurements

We tune the device to a configuration with strong interdot coupling through transport measurements to locate regions in which PMM sweet spots are expected (see Methods). We then isolate the device from the left lead and track the relevant QD resonances while compensating for cross-capacitance. In Fig. 3, we focus on quantum capacitance measurements, as illustrated in Fig. 3a. The corresponding charge-stability diagram is shown in Fig. 3b. At the centre, in which both dots are on resonance ($\mu_{LD} = \mu_{RD} = 0$), we record a time trace of ΔS^{11}_M, which shows discrete switching between two values (Fig. 3c). These switching events reflect transitions between even and odd parity ground states. A two-state hidden Markov model (see Methods) identifies these transitions and yields a characteristic switching time of $\tau_{avg} = 1.85 \pm 0.03$ ms, consistent with fits of the power spectral density and the dwell times statistics (Extended Data Fig. 4). The bimodal histogram (Fig. 3d) confirms single-shot parity readout, with an optimized integration time of 150 µs, giving a 6% minimal readout error and achieving a signal-to-noise ratio $SNR_M = 1$ in 40 µs (see Extended Data Fig. 4). The absence of the excited states suggests fast relaxation within each parity sector, consistent with nanosecond timescales for double QDs[37].

Next we extract the lifetimes τ_e and τ_o of the even and odd parity states. From these, we compute the parity polarization $P_M = (\tau_e - \tau_o)/(\tau_e + \tau_o)$. This quantity indicates the probability of finding the system in either parity state: near zero implies that both are equally likely, whereas positive or negative values indicate an imbalance. We measure P_M across a grid of chemical potentials around the joint charge degeneracy (dotted grey box in Fig. 3b), producing the map shown in Fig. 3e. The polarization varies with dot energies, reaching near zero at the centre, in which dot levels align. Linecuts along the diagonal and anti-diagonal directions show a quadratic variation near the centre, consistent with previous observations in minimal Kitaev chains in which the energy splitting grows quadratically with detuning. This behaviour can be understood by modelling the system as coupled to a hot reservoir of fermions[21,38] (see Methods). In this model, the system switches between parity states with rates that depend on their energy. The state with lower energy lives longer, so the observed polarization reflects the energy difference between the two states. Apart from the switching between QD parity states detected along the anti-diagonal, hybridization of the dot levels with an ABS in the hybrid segment produces detectable switching in the top-right corner of the map (see Methods).

We test the robustness of this approach by varying V_H, which tunes the CAR and ECT strengths between the dots. As shown in Extended Data Fig. 5, the shape of the polarization region evolves with V_H, resembling the transition between CAR and ECT observed in transport measurements. This suggests that polarization mapping can indicate sweet spot conditions even when the device is isolated. For Fig. 3, we chose $V_H = 1.665$ V, at which the polarization approaches zero near the centre of the charge-stability diagram, consistent with a PMM sweet spot. Transport measurements after reconnecting the left lead confirm a sweet spot nearby, at $V_H = 1.675$ V (Extended Data Fig. 6).

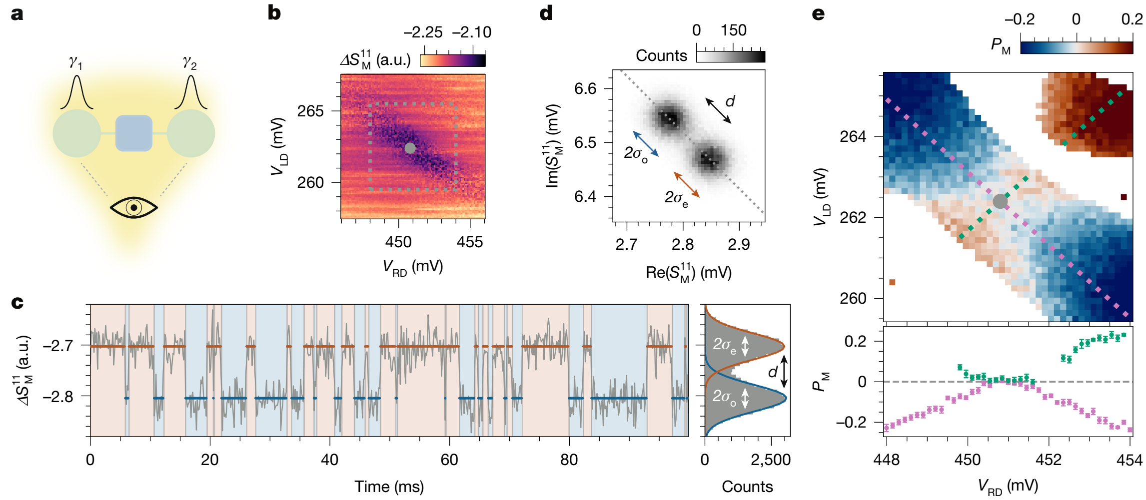

Fig. 3 | Time-resolved parity switching by quantum capacitance. a, Illustration of quantum capacitance readout, which couples to both Majoranas and is sensitive to their parity. **b**, Charge-stability diagram of QDL and QDR measured through ΔS_M^{11} in arbitrary units (a.u.). Random telegraph noise near the anti-diagonal resonance reflects real-time parity switching. **c**, Time trace of ΔS_M^{11} recorded near the centre of the charge-stability diagram (V_{LD} = 262.4 mV and V_{RD} = 450.8 mV; grey dot in **b** and **e**), showing discrete switching events between parity states. For this trace, an integration time of 150 µs is used, which yields $\mathrm{SNR}_M = 1.958 \pm 0.006$ and readout error of 6%. States are assigned and highlighted in colour using a hidden Markov model, which yields $\tau_e = 1.82 \pm 0.05$ ms and $\tau_o = 1.88 \pm 0.04$ ms. The side panel shows count histograms along the principal component axis. Methods for data acquisition and analysis are described in the Methods section 'Time traces measurement and analysis'. **d**, Histogram of complex S_M^{11} from the time trace in **c**. The separation d and standard deviations σ_e and σ_o of the distributions are used to calculate the signal-to-noise ratio $\mathrm{SNR} = d/(\sigma_e + \sigma_o)$. The dotted line indicates the principal component axis along which the data are projected. **e**, Top, map of parity polarization P_M around the joint charge degeneracy inside the dotted grey box of **b**, derived from 10-s time traces. Only pixels for which $\mathrm{SNR}_M \geq 0.5$ are included (see also Methods and Extended Data Fig. 5). Bottom, linecuts of P_M along the diagonal (green) and anti-diagonal (pink) directions in the top panel, showing approximately quadratic dependence consistent with energy detuning of PMMs from the sweet spot.

PMM charge neutrality

Next we compare two complementary measurements of the Kitaev chain: quantum capacitance readout by the superconducting lead and charge sensing by a nearby QD (characterized in Extended Data Fig. 7). Time traces of both signals were recorded simultaneously (Fig. 4a). Near the centre of the charge-stability diagram, parity switching appears only in the quantum capacitance signal (Fig. 4b). The superconducting probe couples the two PMMs through charge fluctuations on both dots and therefore resolves their parity, whereas the CS remains insensitive because both parity states produce the same average charge on QDR[3].

Detuning the left dot shifts its PMM towards the right, so that both PMMs overlap on QDR[4,39] and the CS becomes sensitive to their parity. As such, both the quantum capacitance and the CS can detect switching events (Fig. 4d). Their signals are strongly correlated, meaning that both sensors detect the same transitions. We quantify this using the Pearson correlation coefficient $\rho_{MR} \approx 0.85$, in which $\rho_{MR} = +1$ indicates perfect correlation and $\rho_{MR} = -1$ perfect anticorrelation. We attribute imperfect correlations to limited SNR outside optimal operating regimes (see Methods).

Figure 4c shows a full map of the correlation coefficient, which is strongest where both sensors clearly detect parity switching and vanishes where either sensor is insensitive. Notably, the sign of the correlation flips between the top and bottom halves of the map. This occurs because the global parity of the ground state changes as QDL crosses its charge transition, whereas the local parity of QDR remains fixed. The quantum capacitance reflects this change, as it senses the combined state of both dots, whereas the CS responds only to the charge on QDR. As a result, the two measurements respond in opposite ways to the same parity-switching events, leading to anticorrelation (Fig. 4e).

At the centre of the charge-stability diagram, the correlation coefficient crosses through zero. Here the CS becomes insensitive to the parity state because both parity branches produce the same average charge on QDR. In this situation, switching between even and odd states no longer causes a detectable change in the charge sensing signal. We predict that this condition occurs along the line $\mu_{LD} = \frac{\Delta - t}{\Delta + t}\mu_{RD}$, which becomes horizontal ($\mu_{LD} = 0$) at the PMM sweet spot ($t = \Delta$), as explained in detail in Methods. In our data, the zero-correlation line (black arrows in Fig. 4c) aligns with this prediction. At other V_H values, the line tilts, consistent with detuning from the sweet spot. Also, the width of this line reflects the strength of the couplings and, by extension, the gap to the excited states of the chain (see Extended Data Figs. 5, 8 and 9 for experimental examples and Methods and Extended Data Fig. 10 for theory).

Discussion and conclusion

To implement parity readout in a minimal Kitaev chain, we combined complementary measurement strategies of charge sensing, parity polarization and transport to guide device tuning. These tools consistently indicate operation near the PMM sweet spot, although readout remains sensitive to parity even away from degeneracy. In future qubit implementations, any residual energy splitting $E_M = |t - \Delta|$ would manifest as coherent parity oscillations, allowing optimal fine-tuning by Ramsey-type spectroscopy[11,40,41].

The readout technique introduced here is designed for integration into qubit architectures. In the geometry of two Kitaev chains connected by means of a shared superconductor, each chain contributes a parity-dependent quantum capacitance, as demonstrated in Extended Data Fig. 11. This enables the single-shot discrimination of the qubit basis states and detects leakage from the computational subspace[41]. The method also applies to longer chains, for which detuning all but two dots effectively reduces the system to a minimal chain during readout. Furthermore, we observe that the resonator drive can bias the parity distribution (Extended Data Fig. 4a,b), suggesting a path towards parity initialization by dynamical polarization[42].

This work overcomes a key challenge in realizing Majorana-based qubits by enabling fast, high-fidelity, single-shot parity readout. Although similar functionality has recently been demonstrated using interferometric techniques in extended hybrid devices[23,24],

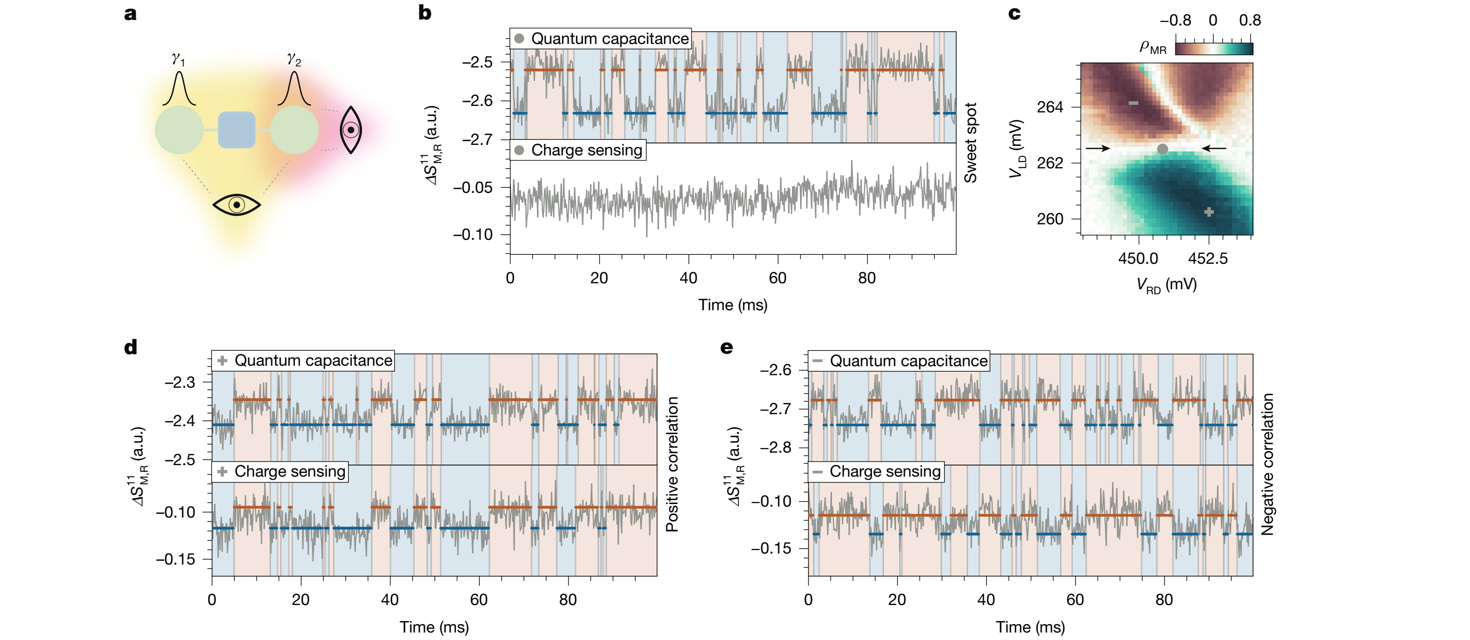

Fig. 4 | Parity readout by means of quantum capacitance and charge sensing. **a**, Schematic of the dual readout set-up: parity is detected by means of quantum capacitance $\Delta S^{11}_{\mathrm{M}}$ and charge by means of a nearby CS $\Delta S^{11}_{\mathrm{R}}$ in arbitrary units (a.u.). **b**, Time traces recorded near the sweet spot (grey dot in **c**, $V_{\mathrm{LD}} = 262.5$ mV and $V_{\mathrm{RD}} = 450.8$ mV). Parity switching is observed in the quantum capacitance signal, whereas the CS does not distinguish parity ($\rho_{\mathrm{MR}} \approx 0.03$). **c**, Map of the Pearson correlation coefficient ρ_{MR} across the charge-stability diagram of QDL and QDR, calculated between the state assignment of the two signals. The correlation vanishes near a horizontal line highlighted by black arrows ($V_{\mathrm{LD}} = 262.5$ mV), consistent with $t \approx \Delta$. **d**, Time traces recorded away from degeneracy (grey '+' in **c**), at which both signals resolve switching events with strong correlation ($\rho_{\mathrm{MR}} \approx 0.85$). **e**, Time traces in the anticorrelated regime (grey '−' in **c**). Switching appears in both signals but with opposite sign, reflecting parity inversion without a change in local parity ($\rho_{\mathrm{MR}} \approx -0.81$).

those approaches require substantial alterations to the device layout and introduce considerable control overhead. By contrast, our method integrates seamlessly with existing device elements, enabling parity readout without added operational complexity. Simultaneous charge sensing verifies charge neutrality, a Majorana signature inaccessible to interferometry. With this capability in place, gate-based control methods become directly applicable. This positions the minimal Kitaev chain as a fully operational platform for time-domain experiments on Majorana fusion, braiding and computation.

Online content

Any methods, additional references, Nature Portfolio reporting summaries, source data, extended data, supplementary information, acknowledgements, peer review information; details of author contributions and competing interests; and statements of data and code availability are available at https://doi.org/10.1038/s41586-025-09927-7.

1. Kitaev, A. Y. Unpaired Majorana fermions in quantum wires. *Phys.-Uspekhi* **44**, 131 (2001).
2. Sau, J. D. & Sarma, S. D. Realizing a robust practical Majorana chain in a quantum-dot-superconductor linear array. *Nat. Commun.* **3**, 964 (2012).
3. Leijnse, M. & Flensberg, K. Parity qubits and poor man's Majorana bound states in double quantum dots. *Phys. Rev. B* **86**, 134528 (2012).
4. Dvir, T. et al. Realization of a minimal Kitaev chain in coupled quantum dots. *Nature* **614**, 445–450 (2023).
5. ten Haaf, S. L. et al. A two-site Kitaev chain in a two-dimensional electron gas. *Nature* **630**, 329–334 (2024).
6. Kitaev, A. Y. Fault-tolerant quantum computation by anyons. *Ann. Phys.* **303**, 2–30 (2003).
7. Nayak, C., Simon, S. H., Stern, A., Freedman, M. & Das Sarma, S. Non-Abelian anyons and topological quantum computation. *Rev. Mod. Phys.* **80**, 1083–1159 (2008).
8. Sarma, S. D., Freedman, M. & Nayak, C. Majorana zero modes and topological quantum computation. *npj Quantum Inf.* **1**, 15001 (2015).
9. Liu, C.-X., Pan, H., Setiawan, F., Wimmer, M. & Sau, J. D. Fusion protocol for Majorana modes in coupled quantum dots. *Phys. Rev. B* **108**, 085437 (2023).
10. Boross, P. & Pályi, A. Braiding-based quantum control of a Majorana qubit built from quantum dots. *Phys. Rev. B* **109**, 125410 (2024).
11. Tsintzis, A., Souto, R. S., Flensberg, K., Danon, J. & Leijnse, M. Majorana qubits and non-Abelian physics in quantum dot–based minimal Kitaev chains. *PRX Quantum* **5**, 010323 (2024).
12. Seoane Souto, R. & Aguado, R. in *New Trends and Platforms for Quantum Technologies* 133–223 (Springer, 2024).
13. Bonderson, P., Freedman, M. & Nayak, C. Measurement-only topological quantum computation. *Phys. Rev. Lett.* **101**, 010501 (2008).
14. Vijay, S. & Fu, L. Teleportation-based quantum information processing with Majorana zero modes. *Phys. Rev. B* **94**, 235446 (2016).
15. Plugge, S., Rasmussen, A., Egger, R. & Flensberg, K. Majorana box qubits. *New J. Phys.* **19**, 012001 (2017).
16. Sau, J. D. & Das Sarma, S. Capacitance-based fermion parity readout and predicted Rabi oscillations in a Majorana nanowire. *Phys. Rev. B* **111**, 224509 (2025).
17. Ménard, G. C. et al. Suppressing quasiparticle poisoning with a voltage-controlled filter. *Phys. Rev. B* **100**, 165307 (2019).
18. Sabonis, D. et al. Dispersive sensing in hybrid InAs/Al nanowires. *Appl. Phys. Lett.* **115**, 102601 (2019).
19. De Jong, D. et al. Controllable single Cooper pair splitting in hybrid quantum dot systems. *Phys. Rev. Lett.* **131**, 157001 (2023).
20. Hays, M. et al. Direct microwave measurement of Andreev-bound-state dynamics in a semiconductor-nanowire Josephson junction. *Phys. Rev. Lett.* **121**, 047001 (2018).
21. Bargerbos, A. et al. Singlet-doublet transitions of a quantum dot Josephson junction detected in a transmon circuit. *PRX Quantum* **3**, 030311 (2022).
22. Hinderling, M. et al. Flip-chip-based fast inductive parity readout of a planar superconducting island. *PRX Quantum* **5**, 030337 (2024).
23. Aghaee, M. et al. Interferometric single-shot parity measurement in InAs–Al hybrid devices. *Nature* **638**, 651–655 (2025).
24. Aghaee, M. et al. Distinct lifetimes for X and Z loop measurements in a Majorana tetron device. Preprint at https://arxiv.org/abs/2507.08795 (2025).
25. Rainis, D. & Loss, D. Majorana qubit decoherence by quasiparticle poisoning. *Phys. Rev. B* **85**, 174533 (2012).
26. Aumentado, J., Keller, M. W., Martinis, J. M. & Devoret, M. H. Nonequilibrium quasiparticles and 2e periodicity in single-Cooper-pair transistors. *Phys. Rev. Lett.* **92**, 066802 (2004).
27. Catelani, G., Schoelkopf, R. J., Devoret, M. H. & Glazman, L. I. Relaxation and frequency shifts induced by quasiparticles in superconducting qubits. *Phys. Rev. B* **84**, 064517 (2011).
28. Karzig, T., Cole, W. S. & Pikulin, D. I. Quasiparticle poisoning of Majorana qubits. *Phys. Rev. Lett.* **126**, 057702 (2021).
29. Contamin, L. C., Delbecq, M. R., Douçot, B., Cottet, A. & Kontos, T. Hybrid light-matter networks of Majorana zero modes. *npj Quantum Inf.* **7**, 171 (2021).
30. Colless, J. et al. Dispersive readout of a few-electron double quantum dot with fast rf gate sensors. *Phys. Rev. Lett.* **110**, 046805 (2013).
31. De Jong, D. et al. Rapid detection of coherent tunneling in an InAs nanowire quantum dot through dispersive gate sensing. *Phys. Rev. Appl.* **11**, 044061 (2019).

32. Vigneau, F. et al. Probing quantum devices with radio-frequency reflectometry. *Appl. Phys. Rev.* **10**, 021305 (2023).
33. Badawy, G. et al. High mobility stemless InSb nanowires. *Nano Lett.* **19**, 3575–3582 (2019).
34. Persson, F., Wilson, C., Sandberg, M., Johansson, G. & Delsing, P. Excess dissipation in a single-electron box: the Sisyphus resistance. *Nano Lett.* **10**, 953–957 (2010).
35. Bruhat, L. et al. Cavity photons as a probe for charge relaxation resistance and photon emission in a quantum dot coupled to normal and superconducting continua. *Phys. Rev. X* **6**, 021014 (2016).
36. van Driel, D. et al. Charge sensing the parity of an Andreev molecule. *PRX Quantum* **5**, 020301 (2024).
37. Petta, J. R., Johnson, A. C., Marcus, C. M., Hanson, M. P. & Gossard, A. C. Manipulation of a single charge in a double quantum dot. *Phys. Rev. Lett.* **93**, 186802 (2004).
38. Nguyen, H. Q. et al. Electrostatic control of quasiparticle poisoning in a hybrid semiconductor-superconductor island. *Phys. Rev. B* **108**, L041302 (2023).
39. Bordin, A. et al. Probing Majorana localization of a phase-controlled three-site Kitaev chain with an additional quantum dot. Preprint at https://arxiv.org/abs/2504.13702 (2025).
40. Luethi, M., Legg, H. F., Loss, D. & Klinovaja, J. From perfect to imperfect poor man's Majoranas in minimal Kitaev chains. *Phys. Rev. B* **110**, 245412 (2024).
41. Pan, H., Das Sarma, S. & Liu, C.-X. Rabi and Ramsey oscillations of a Majorana qubit in a quantum dot-superconductor array. *Phys. Rev. B* **111**, 075416 (2025).
42. Wesdorp, J. et al. Dynamical polarization of the fermion parity in a nanowire Josephson junction. *Phys. Rev. Lett.* **131**, 117001 (2023).

Methods

Device fabrication

The device consists of a 95-nm-diameter InSb nanowire[33] contacted by an Al film that induces superconductivity and is fabricated using a modified shadow-wall lithography technique based on refs. 43,44. The base substrate consists of high-resistivity Si with a 100-nm Si_3N_4 layer grown by low-pressure chemical vapour deposition. Bottom gates (3-nm/7-nm Ti/Pd) were deposited by electron-beam evaporation, with 50-nm W bond pads added by means of RF sputtering. A 20-nm/10-nm Al_2O_3/HfO_2 gate dielectric was grown using atomic layer deposition. To pattern the superconductor, a local shadow mask was created near the fine gate array. The substrate was first coated with poly(methyl methacrylate) (PMMA, 950k A8, about 800 nm thick), exposed using electron-beam lithography (EBL) (500 × 500-nm squares) and developed in MIBK:IPA (1:3). A 600-nm HSQ (FOx-25) layer was then spun on, baked and patterned by EBL to define the superconductor openings. HSQ was developed in MF-21A at 50 °C and PMMA removed in acetone, resulting in suspended masks supported by HSQ pillars. The nanowire is placed using an optical nanomanipulator, followed by hydrogen-radical cleaning in an electron-beam evaporator. A 17.5-nm Al layer was deposited at a 30° angle to form the approximately 180-nm-wide hybrid segment and then oxidized in 200 mtorr O_2 for 5 min. In Extended Data Fig. 2a, we show an example of a nanowire after deposition of the Al film, together with the shadow mask. Following deposition, masks were mechanically removed. The same device after removal of the mask is shown in Extended Data Fig. 2b. To etch excess Al, PMMA (950k A4) was applied, vacuum-cured and patterned by EBL to protect the hybrid section (see Extended Data Fig. 2c). The Al was etched using Transene type D (60 s at room temperature), rinsed in H_2O and resist stripped in acetone. The result is shown in Extended Data Fig. 2d. Finally, ohmic contacts (10-nm/90-nm Cr/Au) were defined by EBL and deposited by electron-beam evaporation. The device in Extended Data Fig. 11 was fabricated using the same recipe. Further fabrication details including substrate preparation, nanowire surface treatment, superconductor growth and ohmic contact fabrication are described in ref. 44.

Measurement set-up

The sample was measured in an Oxford Triton 400 dilution refrigerator with a base temperature of about 20 mK, which is equipped with a 6/1/1 T vector magnet. The contacts to the nanowire are wire-bonded to LC resonators on a separate frequency-multiplexing chip[45]. The spiral inductors bonded to the superconductor and right lead have a nominal inductance of 570 nH and 150 nH, respectively. These resonators enable RF reflectometry by means of voltages V_M^{RF} and V_R^{RF} at the respective resonance frequencies $f_M \approx 340.8$ MHz and $f_R \approx 704.0$ MHz. The superconductor is grounded through a bias tee, whereas DC voltages V_L^{DC} and V_R^{DC} can be applied to the normal leads. We use a Mini-Circuits ZUDC20-83-S+ directional coupler to couple the RF input and output lines. The reflected signal is first amplified by a Cosmic Microwave Technology CITLF3 high-electron-mobility transistor at the 4 K stage and also by a room-temperature amplifier built in-house (M2j module for SPI rack). RF signals are generated and demodulated using a Presto from Intermodulation Products. Infrared filters (XMA 2482-5002CL-CRYO), as well as several layers of shielding, are used to reduce noise and protect the sample from radiation that generates non-equilibrium quasiparticles in the superconducting film. Voltages applied to gate electrodes are controlled using digital-to-analogue converters built in-house. Furthermore, an arbitrary waveform generator built in-house (S5k module for SPI rack) is used to generate sawtooth signals for fast gate sweeps. If their frequency is much smaller than the bandwidth of the DC lines (limited by a second-order RC filter board with 1-kΩ resistors and 1-nF capacitors), they can be summed on top of the DC voltages for fast RF measurements. Two-dimensional measurement data are then obtained all at once (or line by line) instead of point by point, thus reducing the communication-time overhead. Averaging is performed to increase the quality of the signal. Figure 2c and Extended Data Figs. 3, 5a and 6a–c,e–h were measured using the arbitrary waveform generator. Finally, we plot the response of the resonators in two-dimensional measurements by projecting it onto the principal component axis. Further details of the fridge lines and circuitry can be found in Extended Data Fig. 1. The measurements reported in Extended Data Fig. 11 were performed on a similar set-up.

Device tune-up

For tuning up the device, we follow a procedure that is described in ref. 46. The device is controlled using 11 bottom gates that define electrostatic confinement and a parallel magnetic field $B = 150$ mT ensures spin polarization of the QDs[4]. First, we perform transport measurements to confirm the presence of ABSs in the hybrid segment, using V_{LT} and V_{RT} as tunnel barriers. Next we form a pair of QDs QDL and QDR adjacent to the hybrid by confining quantum levels around V_{RD} and V_{LD} with the adjacent gates. We proceed to increase their coupling to the hybrid by lowering the tunnel barrier between them using V_{LT} and V_{RT}, such that the QD levels hybridize with the ABSs. We form the extra QD (CS, controlled with V_{CS}) on the right side that acts as a single-lead CS for QDR[34–36]. We deplete the nanowire between QDR and CS by setting $V_{cut,CS} = -1.2$ V while tracking the QDR and CS resonances. As such, CS is capacitively coupled to QDR without tunnel coupling, whereas residual capacitive coupling to QDL is negligible owing to screening by the superconducting segment[36]. We subsequently take charge-stability diagrams of the QDs with V_{RD} and V_{LD} while adjusting V_H, to observe hybridization between the QD levels. The coupling between QDL and QDR is mediated by the ABSs in the hybrid, with CAR and ECT amplitudes that depend on the hybrid potential and can be balanced by tuning V_H (ref. 4). We use this to identify PMM sweet spots in the transport regime. Finally, we deplete the left part of the nanowire using V_{cut} to isolate the chain from the left lead, while keeping track of QDL's resonance. The device in Extended Data Fig. 11 was tuned up following a similar procedure.

Time traces measurement and analysis

The time traces presented in this work are measured by continuously recording the complex demodulated reflected signal for 10 s, except for Extended Data Figs. 8 and 11, in which we recorded 5-s and 2-s time traces, respectively. The measurement bandwidth is 100 kHz for Fig. 3c,d and Extended Data Fig. 4c–g, 50 kHz for Extended Data Fig. 4a,b, 20 kHz for Figs. 3e and 4 and Extended Data Figs. 5, 7e–i and 9, approximately 17 kHz for Extended Data Fig. 11 and 10 kHz for Extended Data Fig. 8. We analyse each complex time trace by further averaging it in time bins of 150 μs to improve the SNR, unless otherwise specified. Afterwards, we project it onto the principal component axis. To unambiguously determine the principal component vector, we assume its real component to be positive. The resulting one-dimensional time trace is then split into ten subtraces. We fit each subtrace with a two-state hidden Markov model with Gaussian emissions using the Python package hmmlearn. The fitted Markov model assigns the most likely sequence of states to the data and estimates the transition probabilities between them. The two states are then mapped to the physical 'even' and 'odd' states as described in Methods section 'State assignment'. From the transition probabilities $p_{e\to o}$ and $p_{o\to e}$, we calculate the corresponding transition rates as $\Gamma_{e\to o,o\to e} = -\log(1 - p_{o\to e,e\to o})/\tau_{bin}$. These can be used to estimate other relevant quantities, such as the lifetimes $\tau_e = 1/\Gamma_{e\to o}$, $\tau_o = 1/\Gamma_{o\to e}$, $\tau_{avg} = 2/(\Gamma_{e\to o} + \Gamma_{o\to e})$ and the parity polarization $(\tau_e - \tau_o)/(\tau_e + \tau_o)$. Furthermore, the average and standard deviation of the reflected signal can be used to estimate the centre and width of the Gaussians shown in Fig. 3d. Finally, we average the results of each subtrace to estimate the corresponding quantities for the whole time trace. We consider the standard deviation of the mean as their uncertainty. Notably, this analysis relies on the assumption that the switching processes are Poissonian[20]. To verify this, in Extended Data Fig. 4e, we plot the distribution of the dwell times for the time trace discussed in Fig. 3c,d. The fit is in good agreement with an exponential distribution, as expected from a Poissonian process. Furthermore, we note that the choice of integration time can affect the estimation of the parity lifetime, as shown in Extended Data Fig. 4f. Such a systematic error can occur if the integration time is not sufficiently smaller than the typical dwell time[47]. Using a shorter integration time would be detrimental for the SNR and state assignment, as shown in Extended Data Fig. 4c,d.

To further support our analysis, we extract the average switching time of the time trace in Fig. 3c,d using a different procedure that does not require averaging. We divide the unaveraged time trace in ten subtraces and calculate the power spectral density of each subtrace, using Welch's method as implemented in scipy. We fit each power spectral density using a Lorentzian with an extra background:

$$\mathrm{PSD}(f) = 4A\frac{\Gamma_{\mathrm{avg}}}{(2\Gamma_{\mathrm{avg}})^2 + (2\pi f)^2} + B \tag{3}$$

In Extended Data Fig. 4g, we plot the average power spectral density of the ten subtraces. We obtain an average switching time of $\tau_{\mathrm{avg}} = 1/\Gamma_{\mathrm{avg}} = 1.51 \pm 0.07$ ms. This deviates by less than 0.5 ms from the estimation discussed in the main text. Although the finite integration time leads to a systematic error in the lifetime estimation, it does not affect the conclusions of the analysis.

To provide further corroboration, we analyse the time trace of Fig. 3c using the methods and a minimally modified version of the code in ref. 23. The results (Extended Data Fig. 4h,i) are consistent with the hidden Markov model analysis.

Finally, we argue that the imperfect correlation coefficients presented in Fig. 4 can be attributed to suboptimal SNR. To simplify the analysis, we assume that the parity polarization does not greatly deviate from 0. Let X and Y be two telegraph processes whose values can be ±1. If they are perfectly correlated, their correlation is $\rho_{XY} = \langle XY\rangle = 1$. In the presence of assignment errors, the observed signals are X_{obs} and Y_{obs}. If the assignment errors are uncorrelated and their probability is p_X and p_Y, the correlation is $\rho_{X_{\mathrm{obs}}Y_{\mathrm{obs}}} = \langle X_{\mathrm{obs}}Y_{\mathrm{obs}}\rangle = 1 - p_X - p_Y + 2p_X p_Y$. For the positively correlated trace in Fig. 4, we extracted $\mathrm{SNR_M} = 1.27$ and $\mathrm{SNR_R} = 0.97$. The corresponding assignment error is $p_{\mathrm{M}} = [1 - \mathrm{erf}(\mathrm{SNR_M}/\sqrt{2})]/2 \approx 0.10$ and $p_{\mathrm{R}} \approx 0.17$, resulting in an expected correlation of $\rho_{\mathrm{MR}} \approx 0.75$, close to the measured value.

To analyse the time trace measured in a qubit-geometry device (Extended Data Fig. 11g–j), we follow a similar procedure. However, because of the extra complexity of assigning several states, we use a three-state Gaussian mixture model instead of a hidden Markov model. To improve the SNR, we apply a Gaussian filter (100-µs width) rather than a box filter. The lifetimes of the three states and their uncertainties are obtained from the mean dwell times and the standard error of the mean. Transition rates between states i and j are calculated as $\Gamma_{i\to j} = N_{ij}/T_i$, in which N_{ij} is the number of transitions from state i to j and T_i is the total time spent in state i. The uncertainty on the transition rates is estimated as $\sqrt{N_{ij}}/T_i$. If no transitions are observed, we report an upper bound based on the Garwood interval at the 95% confidence level.

State assignment

The two states of the Markov model are mapped to the physical 'even' and 'odd' states using the following procedures.

For the charge sensing measurements, we assume that the state is even at the left of the charge-stability diagram, in which the measured dot is empty. We then use the same mapping for the full charge-stability diagram.

For the quantum capacitance measurements, we assign the states such that the top-left and bottom-right corners of the charge-stability diagram are odd. This mapping is then used for the whole central region, in which the SNR is finite. In the regions with finite SNR that are disconnected from the central region (bottom-left and top-right of the charge-stability diagram), it is the odd state that leads to finite quantum capacitance, as discussed further in Methods section 'Model'. Therefore, we invert the mapping for these regions. Practically, we identify the boundaries of the central region considering the contours $\mathrm{SNR_M} = 0.5$. Beyond these contours, the inverted mapping is used. We include a padding of 3 pixels to account for small inaccuracies in the definition of the boundaries. Although the threshold choice is arbitrary, we find that if $\mathrm{SNR_M} \lesssim 0.5$, the parity polarization varies greatly from pixel to pixel. This suggests that the analysis is not reliable if $\mathrm{SNR_M} \lesssim 0.5$. The same holds for the charge sensing measurements.

Model

In this section, we introduce a phenomenological model of the minimal Kitaev chain and quantum state dynamics, which we compare with experimental findings. First, we assume that the main contribution of CAR and ECT arises from an ABS state residing in the Al-covered part of the semiconductor, which we model as a proximitized resonant level. For simplicity, we neglect the rest of the superconducting continuum, similar to refs. 46,48. This results in the following QD–ABS–QD Hamiltonian,

$$H = H_{\mathrm{QD}} + H_{\mathrm{ABS}} + H_{\mathrm{T}}, \tag{4}$$

$$H_{\mathrm{QD}} = -\mu_{\mathrm{LD}}\, d_{\mathrm{L}}^{\dagger} d_{\mathrm{L}} - \mu_{\mathrm{RD}} d_{\mathrm{R}}^{\dagger} d_{\mathrm{R}}, \tag{5}$$

$$H_{\mathrm{ABS}} = -\mu_{\mathrm{C}} \sum_{\sigma} d_{\mathrm{C}\sigma}^{\dagger} d_{\mathrm{C}\sigma} + \Delta_{\mathrm{P}}(d_{\mathrm{C}\uparrow}^{\dagger} d_{\mathrm{C}\downarrow}^{\dagger} + d_{\mathrm{C}\downarrow} d_{\mathrm{C}\uparrow}) \tag{6}$$

$$H_{\mathrm{T}} = \sum_{j=\mathrm{L/R}} [t_{j\uparrow} d_j^{\dagger} d_{\mathrm{C}\uparrow} + t_{j\downarrow} d_j^{\dagger} d_{\mathrm{C}\downarrow} + \mathrm{h.c.}]. \tag{7}$$

Here d_{L} and d_{R} are annihilation operators for the spin-polarized left/right QDs and $d_{\mathrm{C}\sigma}$ for the central spin-full resonant level, which is proximitized with superconducting pairing Δ_{P}. A small Zeeman splitting is expected for the resonant level, as it is partly screened by the superconductor, which—for simplicity—we neglect in this analysis[48]. Chemical potentials are given by μ_{LD}, μ_{RD} and μ_{C}. Now, by performing a Bogoliubov transformation, $d_{\mathrm{C}\uparrow} = u\beta_{\uparrow} - v\beta_{\downarrow}^{\dagger}$ and $d_{\mathrm{C}\downarrow} = u\beta_{\downarrow} + v\beta_{\uparrow}^{\dagger}$, we obtain,

$$H_{\mathrm{ABS}} = E_{\mathrm{ABS}} \sum_{\sigma} \beta_{\sigma}^{\dagger} \beta_{\sigma}, \tag{8}$$

$$H_{\mathrm{T}} = \sum_{j=\mathrm{L/R}} [t_{j\uparrow} d_j^{\dagger}(u\beta_{\uparrow} - v\beta_{\downarrow}^{\dagger}) + t_{j\downarrow} d_j^{\dagger}(u\beta_{\downarrow} + v\beta_{\uparrow}^{\dagger}) + \mathrm{h.c.}], \tag{9}$$

in which $E_{\mathrm{ABS}} = \sqrt{\mu_{\mathrm{C}}^2 + \Delta_{\mathrm{P}}}$ is the effective gap of the ABS and $u = \frac{1}{\sqrt{2}} \frac{-\Delta_{\mathrm{P}}/E_{\mathrm{ABS}}}{\sqrt{1-\mu_{\mathrm{C}}/E_{\mathrm{ABS}}}}$ and $v = \frac{1}{\sqrt{2}}\sqrt{1 - \mu_{\mathrm{C}}/E_{\mathrm{ABS}}}$ are the coherence factors. The tunnelling, $t_{j\sigma}$, contains spin-dependence owing to spin–orbit interaction. Assuming that both left and right QDs are spin-polarized in the down direction, $d_{\mathrm{L}} = d_{\mathrm{L}\downarrow}$, then $t_{\mathrm{L}\downarrow}$ denotes normal tunnelling and $t_{\mathrm{L}\uparrow}$ denotes spin-flipping tunnelling. Next, to obtain the typical minimal Kitaev chain Hamiltonian, we use quasi-degenerate perturbation theory to trace out the ABS levels and find

$$H_0 = H_{\mathrm{QD}} + \Delta d_{\mathrm{L}}^{\dagger} d_{\mathrm{R}}^{\dagger} + t d_{\mathrm{L}}^{\dagger} d_{\mathrm{R}} + \mathrm{h.c.}, \tag{10}$$

$$\Delta = -\frac{2uv}{E_{\mathrm{ABS}}}(t_{\mathrm{L}\uparrow} t_{\mathrm{R}\downarrow} - t_{\mathrm{L}\downarrow} t_{\mathrm{R}\uparrow}), \tag{11}$$

$$t = \frac{u^2 - v^2}{E_{\mathrm{ABS}}}(t_{\mathrm{L}\uparrow} t_{\mathrm{R}\uparrow} + t_{\mathrm{L}\downarrow} t_{\mathrm{R}\downarrow}), \tag{12}$$

which is valid for $|E_{\mathrm{ABS}} \pm \mu_j| \ll |t_{j\sigma}|$ for j = L/R. To obtain the Majorana zero mode sweet spot from this model, we require $|t| = |\Delta|$, which is fulfilled by $2uv = \pm(t_{\mathrm{L}\uparrow}t_{\mathrm{R}\uparrow} + t_{\mathrm{L}\downarrow}t_{\mathrm{R}\downarrow})/t_{\mathrm{L}}t_{\mathrm{R}}$ with $t_j = \sqrt{t_{j\uparrow}^2 + t_{j\downarrow}^2}$. This yields a gap to the excited states at the sweet spot

$$2|\Delta| = \frac{2t_{\mathrm{L}}t_{\mathrm{R}}}{E_{\mathrm{ABS}}}|2uv(u^2 - v^2)| = \frac{t_{\mathrm{L}}t_{\mathrm{R}}}{E_{\mathrm{ABS}}}|\sin 4\theta|, \tag{13}$$

at chemical potentials $\mu_{\mathrm{LD}} = t_{\mathrm{L}}^2\frac{u^2 - v^2}{E_{\mathrm{ABS}}}$ and $\mu_{\mathrm{RD}} = t_{\mathrm{R}}^2\frac{u^2 - v^2}{E_{\mathrm{ABS}}}$. In the last expression, the angle θ connects to the tunnel couplings in the following way; $t_{\mathrm{L}\uparrow} = t_{\mathrm{L}}\cos\theta$, $t_{\mathrm{R}\uparrow} = t_{\mathrm{R}}\cos\theta$, $t_{\mathrm{L}\downarrow} = t_{\mathrm{L}}\sin\theta$ and $t_{\mathrm{R}\downarrow} = -t_{\mathrm{R}}\sin\theta$ and the gap is maximized if $\theta = \pi/8$. In general however, the ratios $t_{j\uparrow}/t_{j\downarrow}$, and therefore θ, are geometrically set in experiment and not gate-tunable. The primary strategy is therefore to tune μ_{C} by means of electrostatic gating, which tunes u and v, until a sweet spot is observed[4]. In general, both the full Hamiltonian (equation (4)) and the minimal Kitaev Hamiltonian (equation (10)) can be separated into even and odd parity sectors, with $E_{\mathrm{e}n}$ and $E_{\mathrm{o}n}$ denoting the nth excitation in the respective parity sector. For the Kitaev model, the lowest-energy states in each parity are given by $E_{\mathrm{e}0} = -\delta - \sqrt{\delta^2 + \Delta} \equiv E_{\mathrm{e}}^-$ and $E_{\mathrm{o}0} = -\delta - \sqrt{\varepsilon^2 + t^2} \equiv E_{\mathrm{o}}^-$, in which $\delta = (\mu_{\mathrm{LD}} + \mu_{\mathrm{RD}})/2$ and $\varepsilon = (\mu_{\mathrm{LD}} - \mu_{\mathrm{RD}})/2$, with excited states at $E_{\mathrm{e}1} = -2\delta - E_{\mathrm{e}0}$ and $E_{\mathrm{o}1} = -2\delta - E_{\mathrm{o}0}$, which are used in the main text. The theory plots shown in the paper are made by diagonalizing equation (4), to ensure that details of the ABS beyond perturbation are captured, but we exclude the excited ABS singlet state of energy $2E_{\mathrm{ABS}}$ to stay consistent with us neglecting the Bardeen–Cooper–Schrieffer gap of comparable energy. The perturbative model, equation (10), is used to derive minimal equations and gain intuition from the results.

Quantum capacitance and charge sensing. In this subsection, we focus on the primary measures used in the experiment, namely, the signals from quantum capacitance measured on the superconducting lead and charge sensing of the right QD. To derive the quantum capacitance arising from a small oscillating voltage V_{S} on the superconductor, we ask how the energy of state n changes with small fluctuations δV_{S}. Expanding to the second order, we get

$$E_n(V_{\mathrm{S}} + \delta V_{\mathrm{S}}) \approx E_n(V_{\mathrm{S}}) + E_n'(V_{\mathrm{S}})\delta V_{\mathrm{S}} + \frac{1}{2}E_n''(V_{\mathrm{S}})(\delta V_{\mathrm{S}})^2 \tag{14}$$

$$= \frac{1}{2}E_n''(V_{\mathrm{S}})\left(\delta V_{\mathrm{S}} + \frac{E_n'(V_{\mathrm{S}})}{E_n''(V_{\mathrm{S}})}\right)^2 + E_n(V_{\mathrm{S}}) - \frac{1}{2}\frac{E_n'(V_{\mathrm{S}})^2}{E_n''(V_{\mathrm{S}})}, \tag{15}$$

in which, in the second line, we recognize $C_n = E_n''(V_{\mathrm{S}})$ as a capacitance, as it matches the quadratic response $E_{\mathrm{C}} = 1/2C\delta V^2$ of a normal capacitor[49]. We note that this yields the capacitive response of a given state n in a closed system but neglects responses arising from opening the system to a bath, such as decoherence or change of state[50]. We consider this appropriate, as poisoning is slow compared with quantum capacitance measurements. Next, to evaluate E_n'', we consider the effects of δV_{S} on chemical potentials,

$$\mu_j(V_{\mathrm{S}} + \delta V_{\mathrm{S}}) \approx \mu_j(V_{\mathrm{S}}) + (\alpha_{j\mathrm{S}} - 1)e\delta V_{\mathrm{S}}, \Rightarrow \frac{\partial \mu_j}{\partial V_{\mathrm{S}}} = e(\alpha_{j\mathrm{S}} - 1) \tag{16}$$

in which we subtracted $e\delta V_{\mathrm{S}}$, as we measure chemical potentials relative to the superconductor. Here $\alpha_{j\mathrm{S}}$ specifies the lever arm of the superconductor. Physically, $\alpha_{j\mathrm{S}} = 0$ relates to the chemical potentials being completely set by bottom gates, whereas $\alpha_{j\mathrm{S}} = 1$ means that the chemical potentials always match the superconductor, such that δV_{S} imposes no relative change to μ_j. For the ABS, we set $\alpha_{\mathrm{CS}} = 1$, as we assume a strong capacitive coupling to the superconducting lead, thus fixing its chemical potential to the superconductor. For the QDs, $\alpha_{\mathrm{LS}}, \alpha_{\mathrm{RS}} \neq 1$, as the bottom gates primarily set their chemical potential. As such, we obtain

$$\begin{aligned} E_n'' \approx{}& \frac{e^2}{4}(2 - \alpha_{\mathrm{LS}} - \alpha_{\mathrm{RS}})^2\frac{\partial^2 E_n}{\partial \delta^2} + \frac{e^2}{4}(\alpha_{\mathrm{LS}} - \alpha_{\mathrm{RS}})^2\frac{\partial^2 E_n}{\partial \varepsilon^2} \\ &+ \frac{e^2}{2}\frac{\partial^2 E_n}{\partial \delta \partial \varepsilon}(2 - \alpha_{\mathrm{LS}} - \alpha_{\mathrm{RS}})(\alpha_{\mathrm{LS}} - \alpha_{\mathrm{RS}}). \end{aligned} \tag{17}$$

Finally, assuming that lever arms are fairly symmetrical ($\alpha_{\mathrm{LS}} \approx \alpha_{\mathrm{RS}}$) and defining $\alpha = 2 - \alpha_{\mathrm{LS}} - \alpha_{\mathrm{RS}}$, we use the Hellmann–Feynman theorem to rewrite

$$E_n''(V_{\mathrm{S}}) \approx \frac{\alpha^2 e^2}{4}\frac{\partial^2 E_n}{\partial \delta^2} = \frac{\alpha^2 e^2}{4}\frac{\partial}{\partial \delta}\langle n|\frac{\partial H}{\partial \delta}|n\rangle. \tag{18}$$

Here $\partial H/\partial\delta$ is simply the total charge of both QDs (see equation (4)) and we arrive at the quantum capacitance of state n

$$C_n \approx \frac{\alpha^2 e^2}{4}\frac{\partial^2 E_n}{\partial \delta^2} = -\frac{\alpha^2 e^2}{2}\frac{\partial}{\partial \delta}\langle n|d_{\mathrm{L}}^\dagger d_{\mathrm{L}} + d_{\mathrm{R}}^\dagger d_{\mathrm{R}}|n\rangle. \tag{19}$$

Using this equation for the minimal Hamiltonian (equation (10)), the quantum capacitance of the odd states is zero, as both are superpositions of $|01\rangle$ and $|10\rangle$ with a constant total charge of 1. The even ground state yields a signal

$$C_{\mathrm{e}0} = -\alpha^2 e^2 \frac{1}{4}\frac{\Delta^2}{(\delta^2 + \Delta^2)^{\frac{3}{2}}}, \tag{20}$$

corresponding to a minimum around $\delta \approx 0$ of width Δ. We note that $\alpha_{\mathrm{LS}} \neq \alpha_{\mathrm{RS}}$ would also yield a signal for the odd state,

$$C_{\mathrm{o}0} = -(\alpha_{\mathrm{LS}} - \alpha_{\mathrm{RS}})^2 e^2 \frac{1}{4}\frac{t^2}{(\varepsilon^2 + t^2)^{\frac{3}{2}}} \tag{21}$$

along the line $\varepsilon \approx 0$ of width t arising from the second term in equation (17). That this signal is not observed in experiment supports our assumption of $\alpha_{\mathrm{LS}} \approx \alpha_{\mathrm{RS}}$. By comparison, if the resonator was coupled to only one QD, through, for example, the left QD bottom gate, we would expect $\alpha_{\mathrm{RS}} \approx \alpha_{\mathrm{CS}} \approx 1$ and $\alpha_{\mathrm{LS}} \approx 0$, as only μ_{LD} varies relative to the superconductor. This would result in no parity distinguishing signal at the sweet spot, $|\Delta| = |t|$, because $C_{\mathrm{e}0} = C_{\mathrm{o}0}$, highlighting that readout requires coupling of the Majoranas. In Extended Data Fig. 10a, we plot the numerically obtained quantum capacitance signal, assuming $\alpha_{\mathrm{LS}} = \alpha_{\mathrm{RS}}$, in terms of the difference $\delta C_{\mathrm{Q}} = C_{\mathrm{o}0} - C_{\mathrm{e}0}$, which is appropriate as both $C_{\mathrm{e}0}$ and $C_{\mathrm{o}0}$ are strictly negative for equation (4) owing to QD charge monotonically increasing with δ in equation (19). This quantity thus shows which state yields the dominant quantum capacitance signal, whereas areas of $\delta C_{\mathrm{Q}} = 0$ indicate where the states are indistinguishable, that is, yielding signals of equal amplitude. The positive signal along the anti-diagonal $\mu_{\mathrm{LD}} \approx -\mu_{\mathrm{RD}}$ originates from equation (20), whereas the negative corners originate from the odd state hybridizing with the ABS when $E_{\mathrm{ABS}} \approx E_{\mathrm{o}0} - E_{\mathrm{e}0}$, which goes beyond the minimal Kitaev chain Hamiltonian. To quantify how accurate the perturbative PMM model is at the sweet spot, we compare the numerically obtained signal strength, $C_{\mathrm{e}0} - C_{\mathrm{o}0}$, with the perturbative prediction of equation (20), $C_{\mathrm{e}0,\mathrm{per}} - C_{\mathrm{o}0,\mathrm{per}} = -\alpha^2 e^2/4\sqrt{\Delta}$. For parameters $t_{\mathrm{L}} = t_{\mathrm{R}} = 0.5E_{\mathrm{ABS}}$, $\theta = \pi/8$ and $\mu_{\mathrm{C}} = 0.75\Delta_{\mathrm{P}}$ yielding a gap of $|\Delta| \approx 0.125E_{\mathrm{ABS}}$, we find $(C_{\mathrm{e}0,\mathrm{per}} - C_{\mathrm{o}0,\mathrm{per}})/(C_{\mathrm{e}0} - C_{\mathrm{o}0}) \approx 1.1$. This indicates that higher-order terms reduce the signal slightly, on the scale of 10%.

For charge sensing, it is the charge of the right QD that is measured, which, for state n, is given by

$$Q_{\mathrm{R},n} = \langle n|d_{\mathrm{R}}^\dagger d_{\mathrm{R}}|n\rangle. \tag{22}$$

For the minimal Kitaev Hamiltonian, equation (10), this yields the signals

$$Q_{\mathrm{R,e0}} = \frac{\Delta^2}{2\sqrt{\delta^2+\Delta^2}}\frac{1}{\sqrt{\delta^2+\Delta^2}+\delta}, Q_{\mathrm{R,o0}} = \frac{t^2}{2\sqrt{\varepsilon^2+t^2}}\frac{1}{\sqrt{\varepsilon^2+t^2}+\varepsilon}, \quad (23)$$

These quantities are strictly positive and describe an anti-diagonal and diagonal line, respectively, separating plateaus of $Q_R = 1$ from $Q_R = 0$. Subtracting the lines ($\delta Q_R = Q_{R,o0} - Q_{R,e0}$) yields two characteristic triangular shapes, as shown in Extended Data Fig. 10b. To identify the line of indistinguishability with charge sensing, we look for the condition

$$Q_{\mathrm{R,e0}} = Q_{\mathrm{R,o0}} \Rightarrow \Delta\left(\sqrt{\varepsilon^2+t^2}+\varepsilon\right) = t\left(\sqrt{\delta^2+\Delta^2}+\delta\right), \quad (24)$$

which is fulfilled by $\mu_{\mathrm{LD}} = \frac{\Delta-t}{\Delta+t}\mu_{\mathrm{RD}}$. This can be verified by using the corresponding relations $\delta = \Delta\mu_{\mathrm{RD}}/(\Delta+t)$ and $\varepsilon = t\mu_{\mathrm{RD}}/(\Delta+t)$ in equation (24). This equation yields an indicator for the sweet spot, as the criterion of $t = \Delta$ yields a flat line separating the triangles, whereas other choices yield a titled line (Extended Data Fig. 10c–e). This slope also correlates to the width of the δQ_R transitions, for which the anti-diagonal width is given by Δ and the diagonal by t, meaning that the line tilts towards the diagonal of lowest width. Focusing now on the sweet spot ($\Delta = t$), we expand δQ_R around μ_{LD}/Δ for $\mu_{\mathrm{RD}} = 0$, yielding

$$\delta Q_{\mathrm{R}} \approx \frac{-16\Delta\mu_{\mathrm{LD}}}{16\Delta^2+\mu_{\mathrm{LD}}^2}, \quad (25)$$

which corresponds to a Lorentzian with a full width at half maximum of 2Δ. The width of the white indistinguishability line separating the tips of the two triangles in Extended Data Fig. 10c can thus be used to estimate the size of the gap at the sweet spot.

Occupation. Above, we investigated the minimal Hamiltonian and the signals arising from the lowest-energy parity states. Next we wish to tackle the occupation of the even and odd parity states, which goes beyond the closed-system Hamiltonian in equation (4), and provide a minimal description for the observed parity polarizations and parity lifetimes. First, changing parity requires the addition or removal of a quasiparticle from the QD–ABS–QD system, which we assume to be the slowest rate in the system providing the millisecond parity lifetimes. Accordingly, we assume that the intra-parity relaxation rate is much faster[37], such that the system reaches the lowest-energy state in a given parity sector (E_{e0} for even and E_{o0} for odd) between parity-switching events. We thus concentrate only on the parity-changing rates, which we assume to follow Fermi rates

$$\Gamma_{\mathrm{e}\to\mathrm{o}} = \Gamma_{\mathrm{p}} n_{\mathrm{F}}(E_{\mathrm{e0}} - E_{\mathrm{o0}}, T_{\mathrm{p}}) + \Gamma_{\mathrm{p}} n_{\mathrm{F}}(E_{\mathrm{e0}} - E_{\mathrm{o1}}, T_{\mathrm{p}}), \quad (26)$$

$$\Gamma_{\mathrm{o}\to\mathrm{e}} = \Gamma_{\mathrm{p}} n_{\mathrm{F}}(E_{\mathrm{o0}} - E_{\mathrm{e0}}, T_{\mathrm{p}}) + \Gamma_{\mathrm{p}} n_{\mathrm{F}}(E_{\mathrm{o0}} - E_{\mathrm{e1}}, T_{\mathrm{p}}). \quad (27)$$

Here Γ_{p} denotes the rate of poisoning quasiparticles that change the system's parity, $n_{\mathrm{F}}(E, \mathrm{T}) = 1/(1+\exp E/k_{\mathrm{B}}T_{\mathrm{p}})$ the Fermi distribution and T_{p} a phenomenological temperature added to capture smoothness of the parity polarization maps. This modelling is motivated by three observational facts: first, the parity polarizes towards the lowest-energy parity (specifically, towards even parity when $E_{\mathrm{e0}} < E_{\mathrm{o0}}$ and odd parity otherwise), as seen in Fig. 3. Second, the reflected signals S_{M}^{11} and S_{R}^{11} show only signals from two states, meaning that higher-energy states than E_{e0} and E_{o0} are only negligibly occupied. Third, parity lifetimes decrease towards the central degeneracy point, in which the gap is lowest, as seen in Extended Data Fig. 5. This indicates that the excited states E_{e1} and E_{o1} are involved in poisoning processes.

From this model, the probabilities of being in the even and odd states are given by $P_{\mathrm{e}} = \Gamma_{\mathrm{o}\to\mathrm{e}}/(\Gamma_{\mathrm{e}\to\mathrm{o}} + \Gamma_{\mathrm{o}\to\mathrm{e}})$ and $P_{\mathrm{o}} = \Gamma_{\mathrm{e}\to\mathrm{o}}/(\Gamma_{\mathrm{e}\to\mathrm{o}} + \Gamma_{\mathrm{o}\to\mathrm{e}})$, with polarization given by $P_{\mathrm{M}} = P_{\mathrm{e}} - P_{\mathrm{o}}$, which is plotted in Extended Data Fig. 10f–h for different values of t and Δ. The opening and closing of the cross mimics that of spectroscopy and corresponds to experiments shown in Extended Data Fig. 5. Overall, these equations mimic the system being coupled to a metallic bath with rate Γ_{p} and temperature T_{p}. However, this does not result in a thermal equilibrium distribution at T_{p} owing to the assumption of fast intra-parity relaxation, such that only the lowest-energy parity states are populated. For $T_{\mathrm{p}} \to 0$, the system polarizes completely in the lowest-energy parity sector, with constant $\Gamma_{\mathrm{e}\to\mathrm{o}} + \Gamma_{\mathrm{o}\to\mathrm{e}} = \Gamma_{\mathrm{p}}$. In the other limit of $k_{\mathrm{B}}T_{\mathrm{p}} \gg 2\Delta$, a peak in $\Gamma_{\mathrm{e}\to\mathrm{o}} + \Gamma_{\mathrm{o}\to\mathrm{e}} \approx 2\Gamma_{\mathrm{p}}$ occurs at the sweet spot, corresponding to a dip in τ_{avg}, as shown in Extended Data Fig. 10i. This is because of the added transitions, $\Gamma_{\Delta} = \Gamma_{\mathrm{p}} n_{\mathrm{F}}(E_{\mathrm{e0}} - E_{\mathrm{o1}}, T)$ (and $\mathrm{e} \leftrightarrow \mathrm{o}$), to the excited states, which—at the vicinity of the sweet spot—are minimal, $E_{\mathrm{e1}} - E_{\mathrm{e0}} \approx 2\Delta$ and $E_{\mathrm{o0}} - E_{\mathrm{o1}} \approx 2\Delta$, as sketched in Extended Data Fig. 10j. Last, using this model, we can also calculate the average quantum capacitance given by $\langle C\rangle = P_{\mathrm{e}}C_{\mathrm{e0}} + P_{\mathrm{o}}C_{\mathrm{o0}}$, which—for small coupling—is plotted in Fig. 2d.

Data availability

The raw data measured on the device presented in this work are available at https://doi.org/10.4121/227fd419-fded-4a96-ab62-421a0cd57fa5 (ref. 51).

Code availability

The data processing and plotting code and the code used for the theory calculations are available at https://doi.org/10.4121/227fd419-fded-4a96-ab62-421a0cd57fa5 (ref. 51).

43. Heedt, S. et al. Shadow-wall lithography of ballistic superconductor–semiconductor quantum devices. *Nat. Commun.* **12**, 4914 (2021).
44. Mazur, G. P. et al. Spin-mixing enhanced proximity effect in aluminum-based superconductor–semiconductor hybrids. *Adv. Mater.* **34**, 2202034 (2022).
45. Hornibrook, J. M. et al. Frequency multiplexing for readout of spin qubits. *Appl. Phys. Lett.* **104**, 103108 (2014).
46. Zatelli, F. et al. Robust poor man's Majorana zero modes using Yu-Shiba-Rusinov states. *Nat. Commun.* **15**, 7933 (2024).
47. Naaman, O. & Aumentado, J. Poisson transition rates from time-domain measurements with a finite bandwidth. *Phys. Rev. Lett.* **96**, 100201 (2006).
48. Liu, C.-X., Wang, G., Dvir, T. & Wimmer, M. Tunable superconducting coupling of quantum dots via Andreev bound states in semiconductor-superconductor nanowires. *Phys. Rev. Lett.* **129**, 267701 (2022).
49. Secchi, A. & Troiani, F. Theory of multidimensional quantum capacitance and its application to spin and charge discrimination in quantum dot arrays. *Phys. Rev. B* **107**, 155411 (2023).
50. Peri, L., Benito, M., Ford, C. J. & Gonzalez-Zalba, M. F. Unified linear response theory of quantum electronic circuits. *npj Quantum Inf.* **10**, 114 (2024).
51. Zatelli, F. & van Loo, N. Data and code underlying the publication "Single-shot parity readout of a minimal Kitaev chain". Version 3. *4TU.ResearchData* https://doi.org/10.4121/227fd419-fded-4a96-ab62-421a0cd57fa5.v3 (2025).

Acknowledgements This work has been supported by the Dutch Organization for Scientific Research (NWO), Microsoft Corporation Station Q, the Spanish Ministry of Science (grant no. PID2021-125343NB-I00) and the Horizon Europe framework programme of the European Commission through the European Innovation Council Pathfinder grant no. 101115315 (QuKiT). We thank O. W. B. Benningshof and J. D. Mensingh for technical assistance with the cryogenic electronics, F. K. Malinowski for contributing to the design of the experiment, C. X. Liu and S. L. D. ten Haaf for their input on the manuscript, T. Dvir, A. Lombardi, V. P. M. Sietses, F. J. Bennebroek Evertsz, M. Wimmer, J. D. Torres Luna, S. Miles, S. Goswami, S. Roelofs, D. Joshi and A. R. Akhmerov for discussions, J. M. Hornibrook and D. J. Reilly for providing the frequency multiplexing chips and S. Gazibegovic for contribution to nanowire growth.

Author contributions The sample was fabricated by N.v.L. and B.R. Measurements were performed by N.v.L., F.Z. and T.V.C. The experiment was designed by N.v.L., F.Z. and G.W. The data were analysed by N.v.L. and F.Z. The experimental set-up was designed and implemented by N.v.L., F.Z., B.R., G.W. and D.v.D. The manuscript was prepared by N.v.L. and F.Z., with input from all authors. G.W., A.B., D.v.D., Y.Z., W.D.H. and G.P.M. contributed to understanding and interpretation of the data through regular discussions. The project was supervised by L.P.K. Modelling and simulations of the system were carried out by G.O.S. and R.A. The InSb nanowire growth was performed by G.B. and E.P.A.M.B.

Competing interests The authors declare no competing interests.

Additional information

Supplementary information The online version contains supplementary material available at https://doi.org/10.1038/s41586-025-09927-7.

Correspondence and requests for materials should be addressed to Nick van Loo or Leo P. Kouwenhoven.

Peer review information *Nature* thanks the anonymous reviewers for their contribution to the peer review of this work. Peer reviewer reports are available.

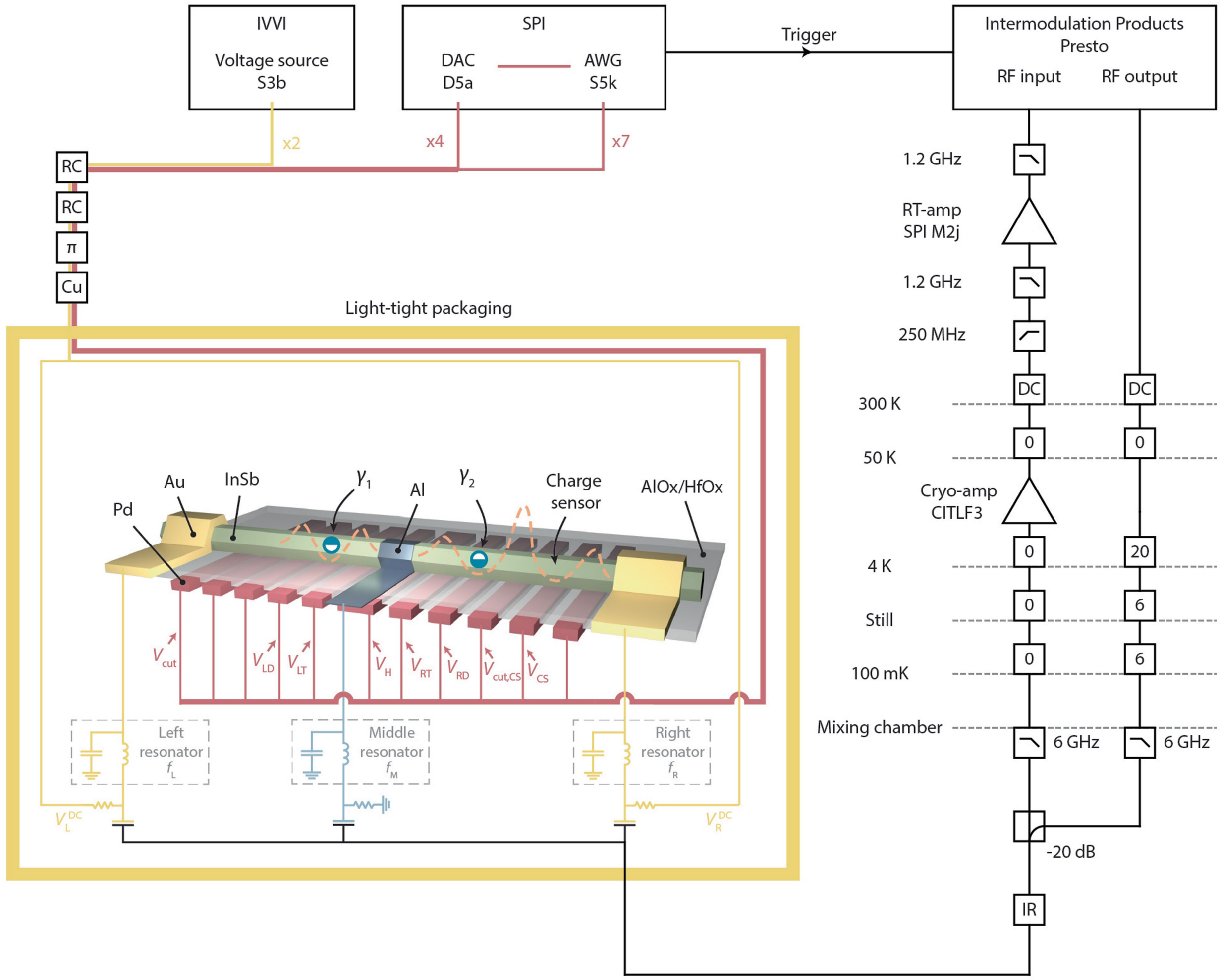

Extended Data Fig. 1 | Measurement set-up. Detailed wiring diagram for the DC and RF lines used to measure the device. To reduce the generation of non-equilibrium quasiparticles in the superconducting film, we use infrared filters for the RF lines. Furthermore, light-tight packaging encloses the device. Finally, we note that an extra resonator was connected to the left normal lead but it was not used.

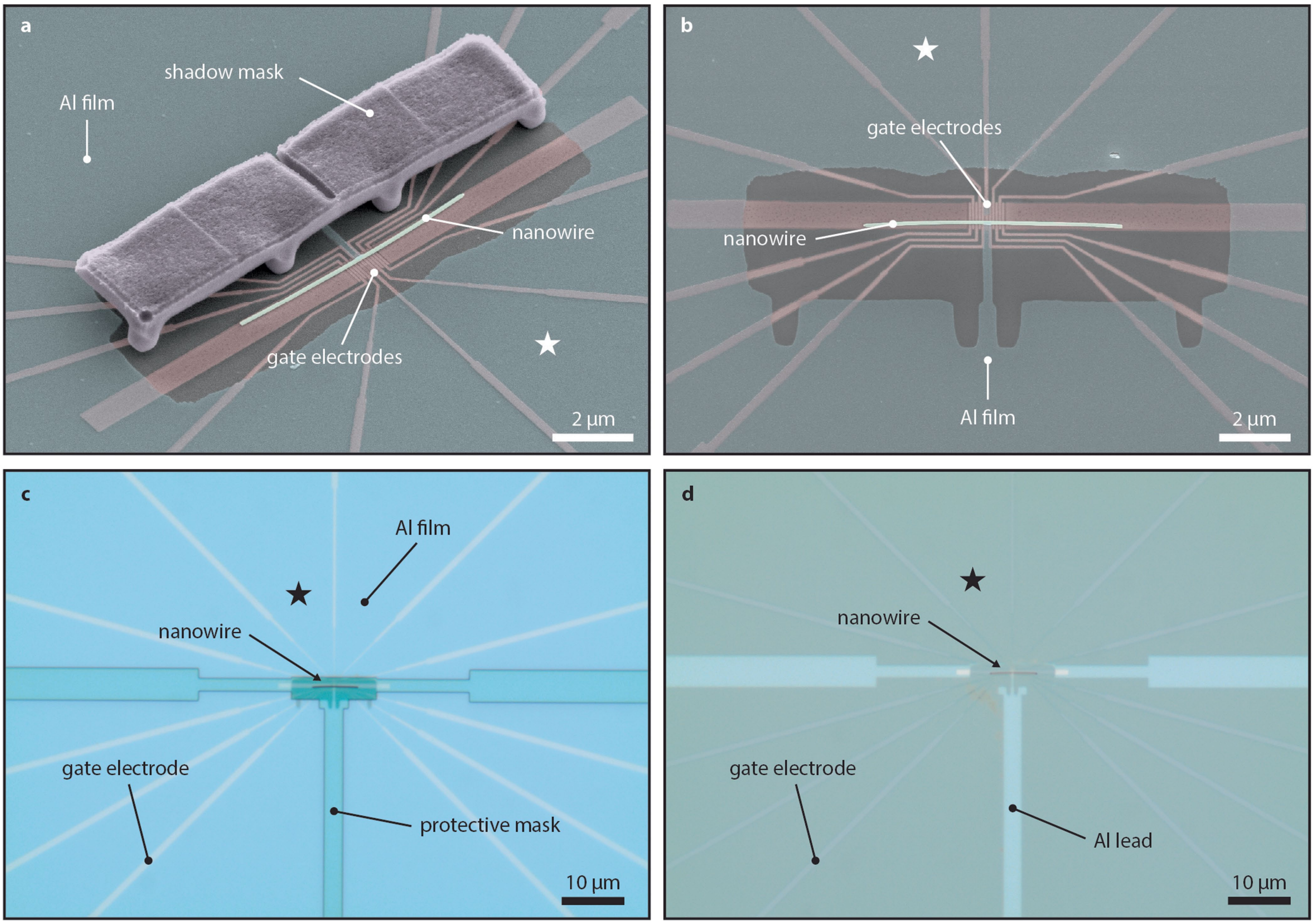

Extended Data Fig. 2 | Shadow lithography with masks grown on-chip. **a**, False-coloured tilted scanning electron micrograph of a nanowire (InSb, shown in green) on top of the gate electrode array (Pd, shown in red) after deposition of the superconductor (Al, shown in blue). The shadow mask (HSQ, shown in purple) has a narrow slit in the centre, through which the Al strip that contacts the nanowire is evaporated, at an angle of 30° with respect to the substrate. A star is placed at approximately the same location in this and the other panels to help identify the orientation of the substrate. **b**, False-coloured top-view scanning electron micrograph of the same nanowire as in panel **a**, after the shadow mask has been mechanically removed using a nanomanipulator. **c**, Optical image of the PMMA mask that covers the nanowire and three leads towards the device. Image taken after patterning and development of the mask but before etching of the Al film using Transene type D. **d**, Optical image of the device after etching of the Al film and stripping of the protective mask. The central Al lead connects the nanowire to a W pad, which facilitates wire bonding (not shown here).

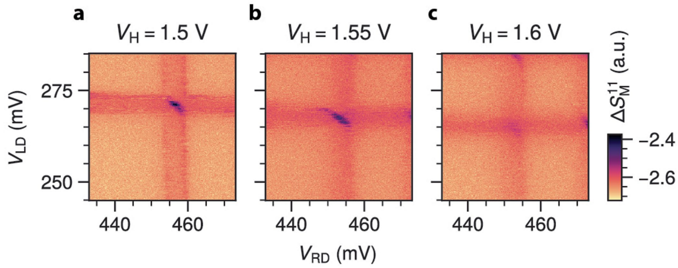

Extended Data Fig. 3 | Evolution of quantum capacitance with hybrid gate voltage V_H. a–c, Quantum capacitance charge-stability diagrams measured using the middle resonator while the device is isolated from the normal leads. Each panel corresponds to a different setting of the hybrid gate voltage V_H, which tunes the energy of the ABS in the superconducting segment. As V_H increases, we observe a progressive weakening of the signal along the interdot detuning axis. This behaviour is attributed to an increase in the strength of CAR between the QDs, mediated by the lowering of the ABS energy. Because quantum capacitance is inversely proportional to CAR strength, a stronger CAR leads to reduced signal contrast. This trend provides a qualitative probe of the CAR amplitude and helps identify regions in which $t \approx \Delta$, as required for the PMM sweet spot.

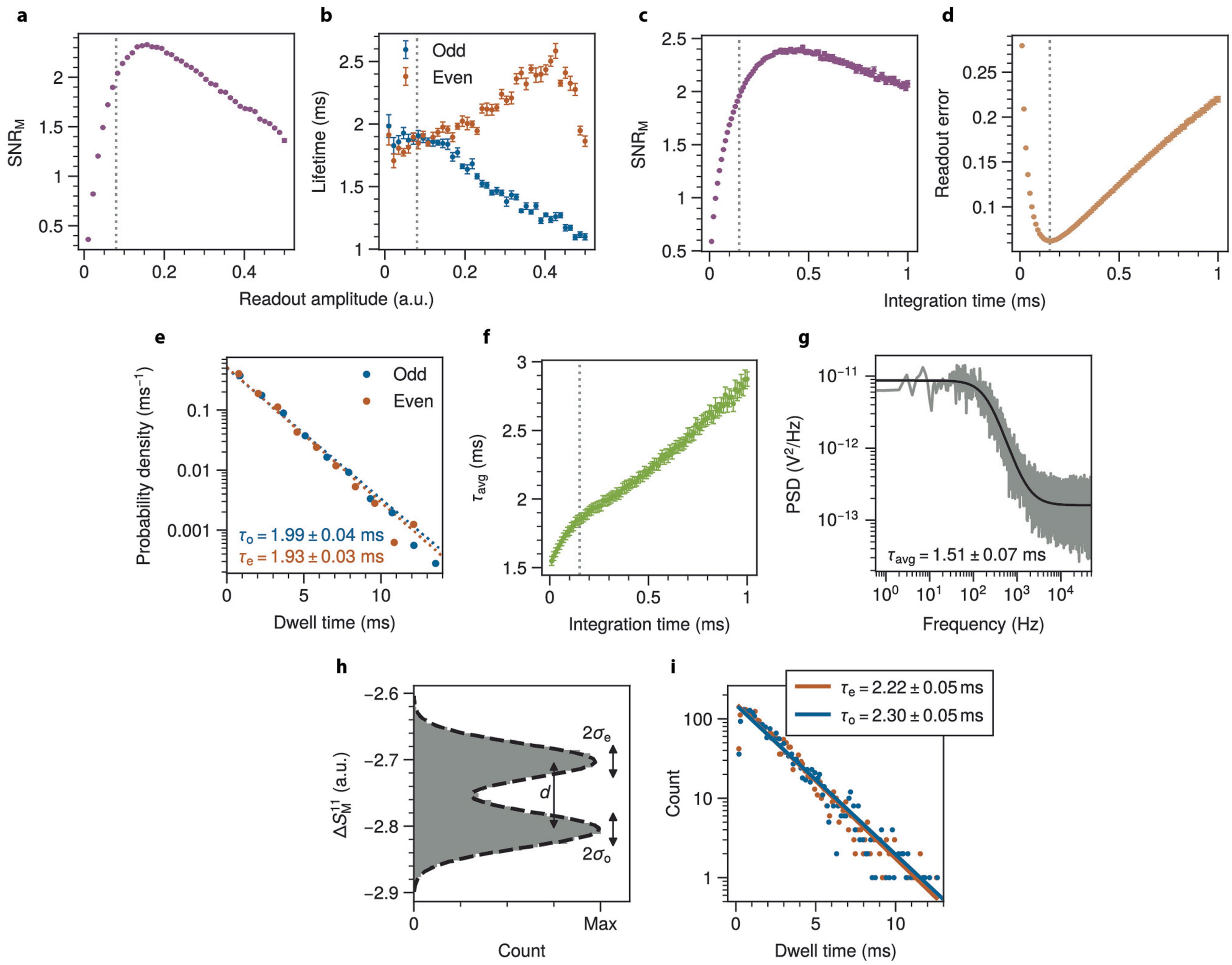

Extended Data Fig. 4 | Detailed analysis of time-trace performance at the PMM sweet spot. a,**b**, Signal-to-noise ratio (SNR_M, panel **a**) and parity lifetimes (panel **b**) as a function of readout amplitude. All data were taken with the same gate settings and 150-μs integration time as in Fig. 3d. The dotted grey line indicates the amplitude used for Figs. 3 and 4. Beyond a certain readout amplitude, the SNR decreases and the lifetimes become parity-dependent, consistent with drive-induced modulation along the common-mode axis δ that preferentially stabilizes the even ground state. This observation suggests that the system can be initialized in the even state by driving the middle resonator with a high amplitude. The time traces in panels **a** and **b** were averaged in time bins of 160 μs (instead of 150 μs) to ensure that the averaging time is an exact multiple of the sampling rate (50 kHz). **c**,**d**, SNR_M (**c**) and readout error (**d**) of the time trace presented in Fig. 3 versus integration time. The readout error was estimated as $[1 - e^{-\tau_{bin}/\tau_{avg}} \mathrm{erf}(SNR_M(\tau_{bin})/\sqrt{2})]/2$ (ref. 23), in which τ_{bin} is the integration time and $\tau_{avg} = 1.85 \pm 0.03$ ms. The dotted grey line indicates the integration time $\tau_{bin} = 150$ μs used for all of the reported measurements unless otherwise specified. **e**, Histograms of dwell times in the even and odd parity states, normalized by total counts. The dotted lines show fits with the corresponding Poissonian probability densities $e^{-t/\tau_{o,e}}/\tau_{o,e}$, confirming that the dwell times follow an exponential distribution. $\tau_{o,e}$ have been estimated as the mean of the dwell times in the odd and even parity states. Their uncertainty has been estimated as the standard deviation of the mean. **f**, Average switching time, τ_{avg}, estimated for varying integration time. As the integration time increases, the estimation of τ_{avg} is systematically biased towards higher values. See Methods section 'Time traces measurement and analysis' for a more detailed discussion. **g**, Power spectral density (PSD) of the time trace using an integration time of 10 μs. By fitting it with a Lorentzian model, we extract an average switching time of 1.51 ± 0.07 ms. The discrepancy between this estimate and those obtained with a hidden Markov model or exponential fitting further suggests that the long integration time needed to obtain high SNR could systematically bias the estimation of τ_{avg}. See Methods section 'Time traces measurement and analysis' for a more detailed discussion. **h**,**i**, Analysis of the time trace of Fig. 3c using the analysis methods and code adapted from ref. 23. In panel **h**, the histogram is fit to a weighted sum of Gaussian distributions. The extracted $SNR = d/(\sigma_e + \sigma_o) = 1.93$ is comparable with the hidden Markov model analysis. In panel **i**, the dwell time distributions are extracted using a Gaussian mixture model and a thresholding algorithm. The parity lifetimes are then estimated by fitting the distributions with an exponential model. The estimates are comparable with those obtained with the hidden Markov model analysis.

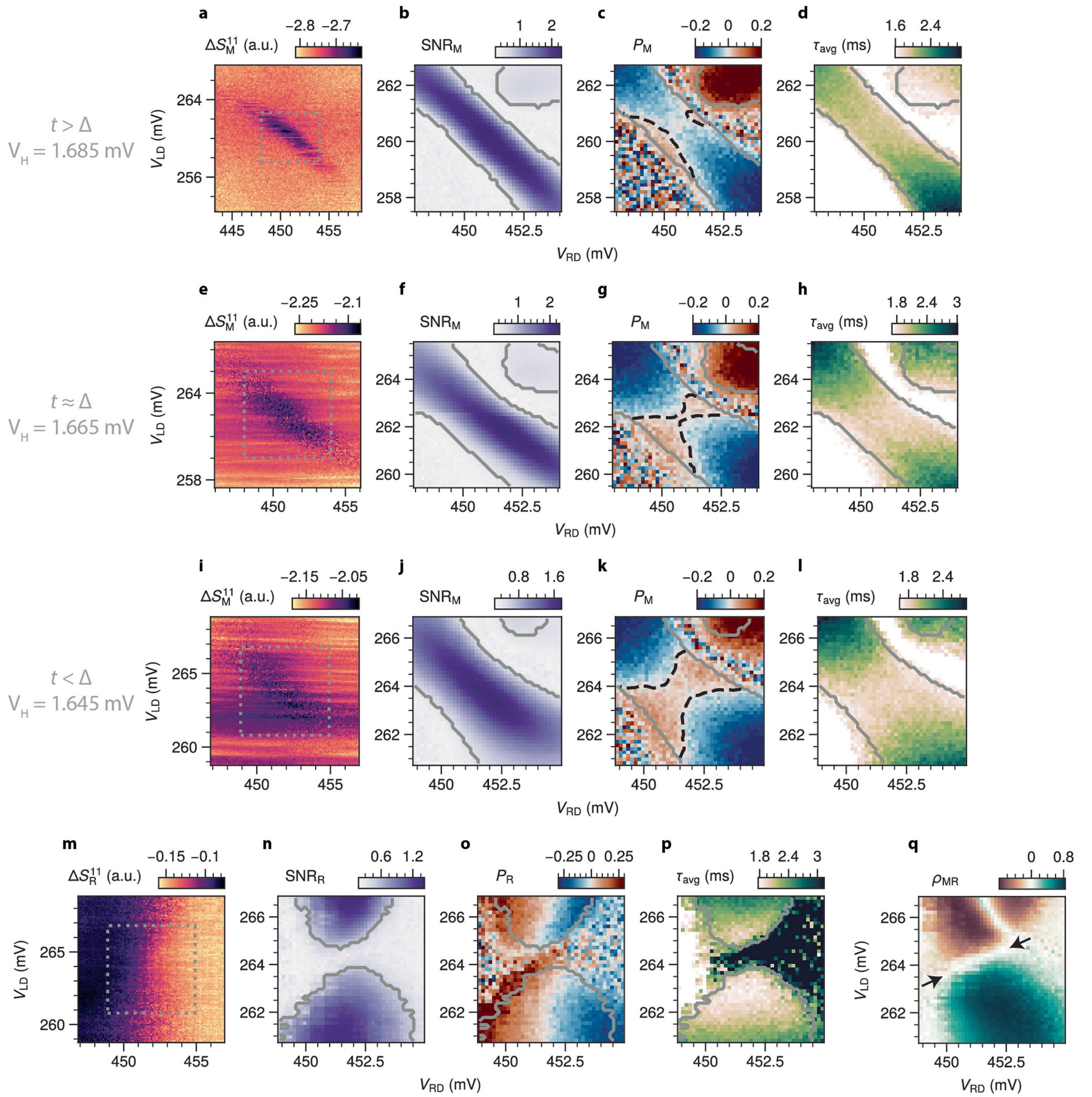

Extended Data Fig. 5 | Evolution of charge-stability diagrams and switching behaviour across the ECT-to-CAR transition. a–d, Measurements at $V_H = 1.685$ V, in which $t > \Delta$. The charge-stability diagram measured by quantum capacitance (**a**) shows strong signal along the detuning axis. The dotted grey dotted box marks the region in which 10-s time traces were measured to estimate (Methods section 'Time traces measurement and analysis') the signal-to-noise ratio (SNR_M, panel **b**), parity polarization (P_M, panel **c**) and average switching time (τ_{avg}, panel **d**). In these panels, the grey contours indicate where $SNR_M = 0.5$. In panel **c**, a dashed black line highlights the contour at which $P_M = 0$, calculated after applying a Gaussian filter with standard deviation of 1 pixel to reduce noise. This contour resembles an avoided crossing along the detuning axis, characteristic of the condition $t > \Delta$. **e–h**, Same measurements at $V_H = 1.665$ V, in which $t \approx \Delta$ near the PMM sweet spot. In this case, the parity polarization map (panel **g**) shows no avoided crossing. Instead, regions of positive and negative parity polarization alternate around the centre of the charge-stability diagram, indicating that CAR and ECT are balanced. This is the dataset used in the main text. **i–l**, Same at $V_H = 1.645$ V, at which CAR dominates ($t < \Delta$). Here the polarization map (panel **k**) shows that the avoided crossing reappears but now along the common-mode axis, reversing the pattern seen in **c**. This indicates that the system transitioned to a regime in which $t < \Delta$. **m–p**, Corresponding data from panels **i–l** using the CS, recorded by the right resonator. The SNR_R vanishes at the centre of the charge-stability diagram, when the QDL is on resonance ($V_{LD} \approx 264$ mV). This indicates that a charge measurement of QDR is not sufficient to determine the parity of the system. **q**, Map of the Pearson correlation coefficient ρ_{MR} between quantum capacitance and CS signals in the $t < \Delta$ regime. The sign change of ρ_{MR} (black arrows) no longer follows a horizontal line. This is consistent with CAR dominating over ECT, as explained in more detail in Methods section 'Model'.

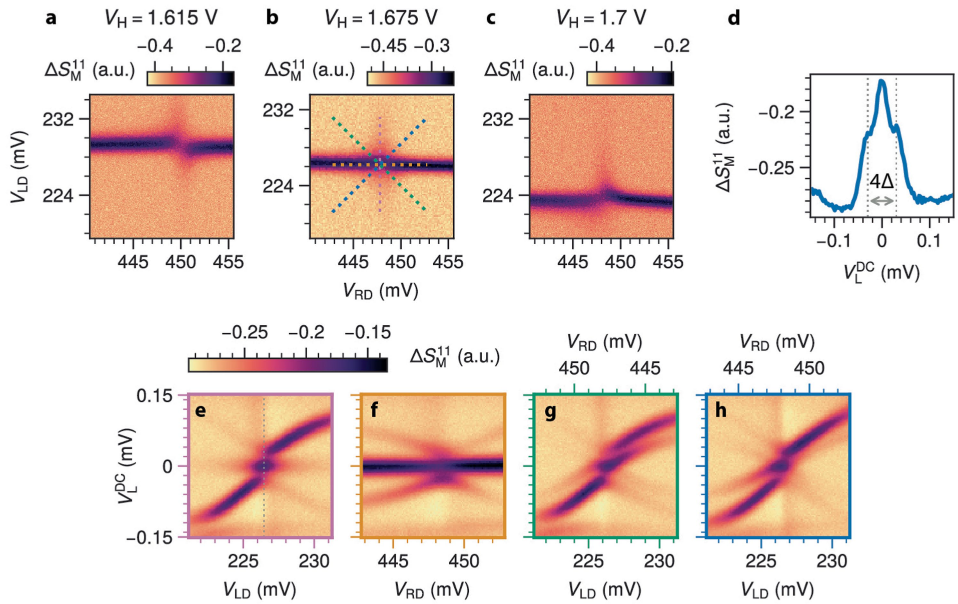

Extended Data Fig. 6 | Transport measurement of the PMM sweet spot using RF reflectometry. a–**c**, Zero-bias charge-stability diagrams for different values of V_H, used to tune the relative strength of ECT and CAR. In all panels, the left lead is operated as a tunnel probe, whereas the right side is blocked by the CS. As a result, transport occurs predominantly through QDL and visibility of the QDR resonance is suppressed. The orientation of the avoided crossing in panel **a** indicates that $t < \Delta$. As V_H increases, the avoided crossing first disappears when the sweet spot $t \approx \Delta$ (**b**) is approached. Further increasing V_H opens the avoided crossing in the opposite direction, indicating that $t > \Delta$ (**c**). The dotted lines in panel **b** indicate the axes along which the spectra of panels **e**–**h** were measured. **d**, Tunnel spectroscopy varying V_L^{DC} at the centre of the charge-stability diagram of panel **b**. The spectrum exhibits a zero-bias peak separated from two excited states by a gap of about 30 μeV, consistent with PMMs in a minimal Kitaev chain. This linecut was extracted along the dotted grey dotted line of panel **e**. **e**,**f**, Spectra measured while varying V_L^{DC} and the electrochemical potential of the left (**e**) or right (**f**) QD. The stable zero-bias peak indicates robustness against local perturbations. **g**,**h**, Spectra measured while varying V_L^{DC} and the electrochemical potential of both QDs along the common-mode (**g**) and detuning (**h**) axis. The zero-bias peak splits quadratically, illustrating limited protection against global perturbations.

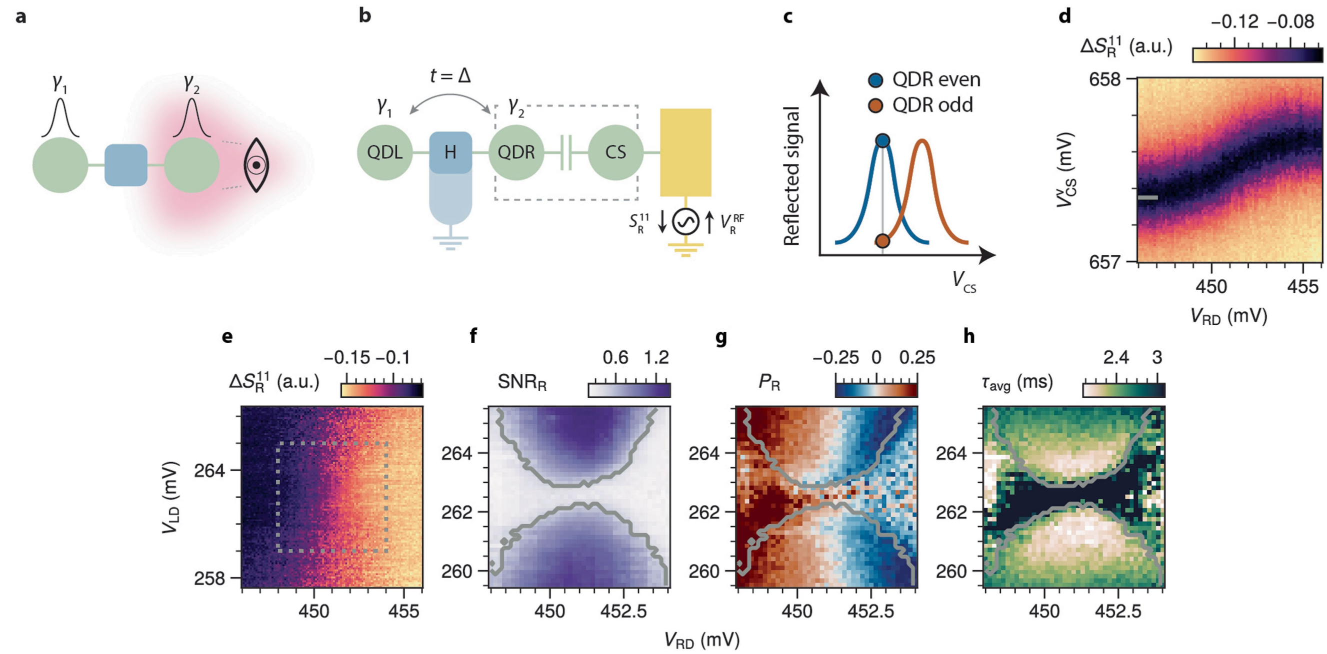

Extended Data Fig. 7 | Parity readout using a nearby CS. a, Illustration showing that a probe that does not couple the two Majoranas to each other cannot access the parity $i\gamma_1\gamma_2$, and is thus insensitive to the stored quantum information. **b**, Schematic of the charge sensing readout. A nearby QD (CS) is capacitively coupled to QDR but isolated by a high tunnel barrier that prevents direct tunnelling between them. A lead with a resonator is coupled to the CS for fast single-lead RF reflectometry[34]. **c**, Principle of charge sensing: changes in the charge on QDR alters the local electrostatic environment, shifting the CS resonance and modulating the reflected signal ΔS_R^{11}. **d**, Charge-stability diagram of QDR and CS measured through ΔS_R^{11}, with QDL held on resonance ($V_{LD} = 263$ mV). To correct for cross-capacitance, the voltage on V_{CS} is adjusted during V_{RD} sweeps, resulting in an effective compensated axis V_{CS}^{v} that is a linear combination of V_{RD} and V_{CS}. **e**, Charge-stability diagram of QDL and QDR with V_{CS}^{v} fixed (grey mark in panel **d**). Outside the QDL resonance, QDR shows fixed charge when its energy is above the hybrid gap E_{ABS}. Below this gap, parity switching is visible as signal noise. Near the QDL resonance ($V_{LD} = 263$ mV), the region of visible switching is reduced when QDL becomes lower in energy than QDR. **f**–**h**, The signal-to-noise ratio (SNR_R, panel **f**), parity polarization (P_R, panel **g**) and average switching time (τ_{avg}, panel **h**) obtained from time traces measured in the dotted grey box of panel **e**. In these panels, the grey contours indicate where $SNR_R = 0.5$. The SNR_R vanishes at the centre of the diagram (in which $V_{LD} \approx 262.5$ mV), indicating that the CS is insensitive to the parity states at this point. This dataset was acquired simultaneously with the quantum capacitance measurements in Fig. 3e and used to compute correlations in Fig. 4.

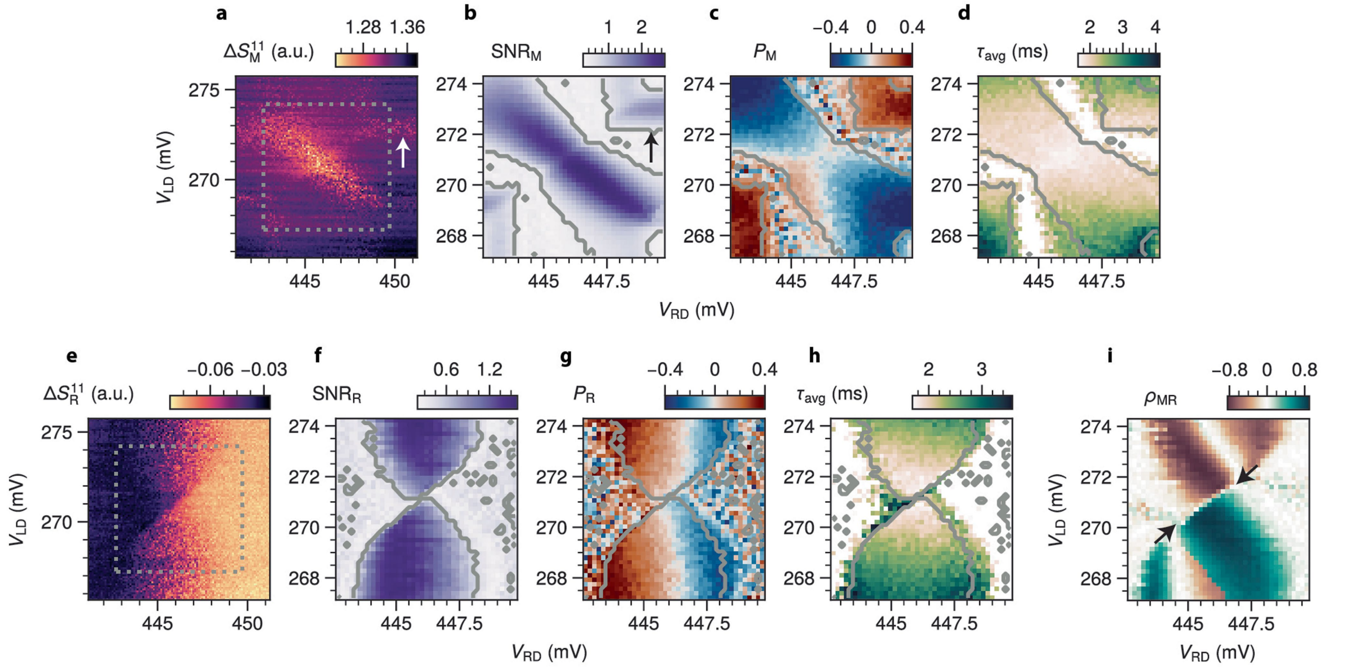

Extended Data Fig. 8 | Time traces with weakly coupled QDs. a–d, Charge-stability diagram measured by quantum capacitance (panel **a**) in a weak interdot coupling regime (V_H = 1.445 V). The dotted grey box marks the region in which time traces were measured to estimate the signal-to-noise ratio (SNR$_M$, panel **b**), parity polarization (P_M, panel **c**) and average switching time (τ_{avg}, panel **d**). We infer the weak coupling from the presence of signal when a QD is aligned to the lowest-energy state in the hybrid, as highlighted by the arrows in panels **a** and **b** and discussed in Fig. 2. In these panels, the grey contours indicate where SNR$_M$ = 0.5. The probing frequency for the middle resonator was 341 MHz instead of 340.8 MHz, as in the rest of the text. The time traces in this figure were averaged in time bins of 200 µs (instead of 150 µs) to ensure that the averaging time is an exact multiple of inverse of the sampling rate (10 kHz). **e–h**, Same measurements by charge sensing. Charge-stability diagram of QDL and QDR (panel **e**). Outside the QDL resonance, QDR shows fixed charge when its energy is above the hybrid gap E_{ABS}. Below this gap, parity switching is visible as signal noise. Near the QDL resonance, the region of visible switching is reduced when QDL becomes lower in energy than QDR. The region in which even and odd states are indistinguishable is narrower than in Extended Data Figs. 7 and 9, consistent with small coupling between QDs (see Methods section 'Model'). **i**, Pearson correlation coefficient between time traces measured with quantum capacitance and charge sensing. Similarly to Extended Data Fig. 5q, the transition region between positive and negative correlation (black arrows) is tilted. Furthermore, this transition is more sharply defined, in line with the low coupling (see Methods section 'Model').

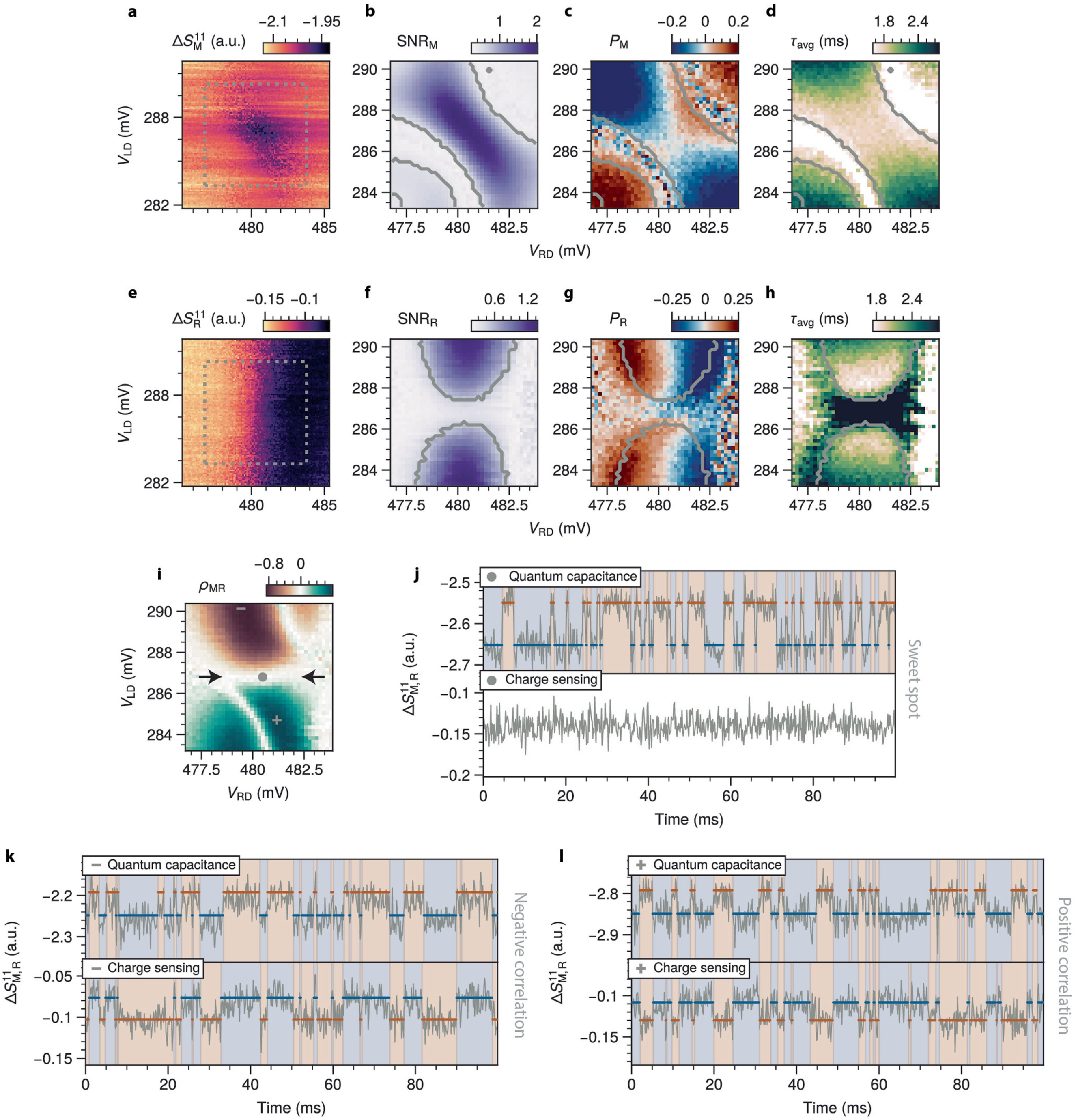

Extended Data Fig. 9 | PMM sweet spot reproduction with different QD resonances. a–**d**, Charge-stability diagram at $V_H = 1.625$ V measured by quantum capacitance (panel **a**), with the corresponding signal-to-noise ratio (SNR$_M$, panel **b**), parity polarization (P_M, panel **c**) and average switching time (τ_{avg}, panel **d**) for different QD resonances in which $t \approx \Delta$. Panels **b**–**d** were measured inside the dotted grey dotted box of panel **a**. In these panels, the grey contours indicate where SNR$_M$ = 0.5. **e**–**h**, Same measurements by means of charge sensing. The charge-stability diagram of QDL and QDR is shown in panel **e**. Outside the QDL resonance, QDR shows fixed charge when its energy is above the hybrid gap E_{ABS}. Below this gap, parity switching is visible as signal noise. Near the QDL resonance ($V_{LD} = 286.8$ mV), the region of visible switching is reduced when QDL becomes lower in energy than QDR. The signal-to-noise ratio (SNR$_R$, panel **f**), parity polarization (P_R, panel **g**) and average switching time (τ_{avg}, panel **h**) are obtained from time traces measured in the dotted grey box of panel **e**. In these panels, the grey contours indicate where SNR$_R$ = 0.5. The region in which SNR$_R$ vanishes near the centre of the diagram is wider than for Extended Data Figs. 7 and 8, indicating a stronger coupling. **i**, Pearson correlation coefficient between time traces measured with quantum capacitance and charge sensing. The black arrows indicate the region in which the CS is insensitive to parity-switching events, resulting in vanishing correlation between time traces measured with quantum capacitance and charge sensing. As for Fig. 4, this line is horizontal ($\mu_{LD} = 0$), which occurs only at the PMM sweet spot ($t = \Delta$). **j**–**l**, Examples of uncorrelated (**j**), negatively correlated (**k**) and positively correlated (**l**) time traces. The marks in panel **i** indicate the specific gate values at which these time traces were measured. Note that, for panels **k** and **l**, the reflected signal is, respectively, positively and negatively correlated, opposite to the state assignment (see Methods section 'State assignment' for more details).

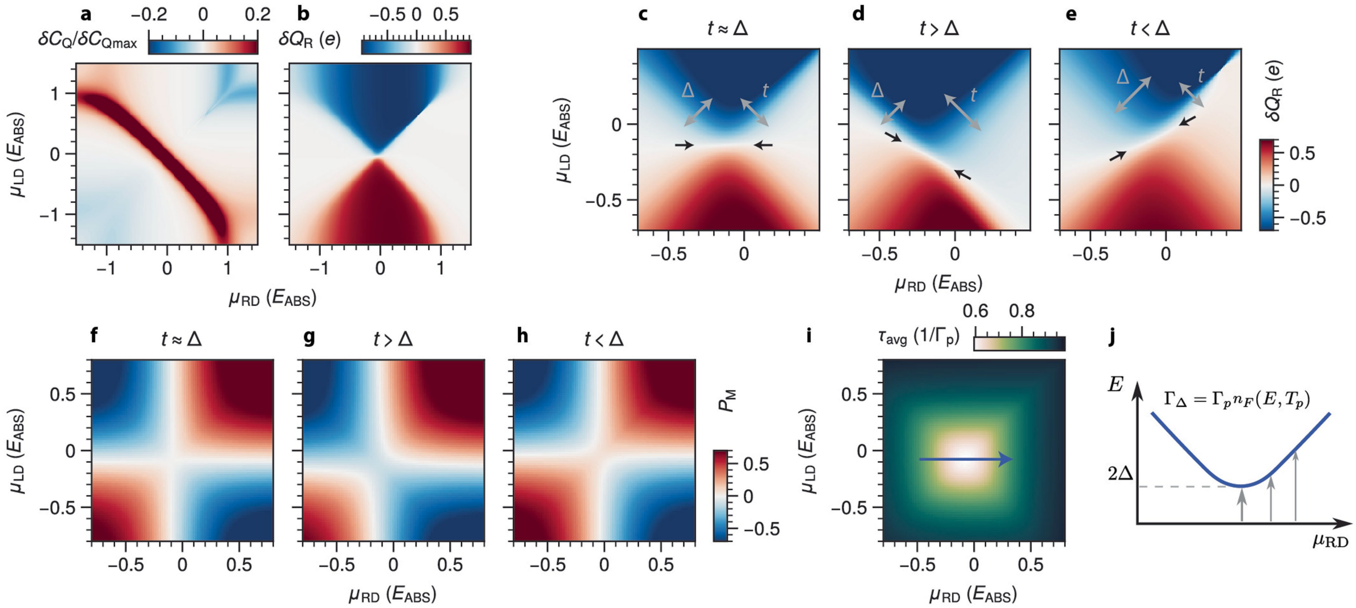

Extended Data Fig. 10 | Theory model of quantum capacitance, charge sensing and quasiparticle poisoning dynamics. a,**b**, Quantum capacitance (**a**) and right QD charge difference (**b**) for $t_L = t_R = 0.3E_{ABS}$, $\theta = \pi/8$ and $\mu_C = 0.75\Delta_P$, corresponding to a PMM sweet spot. Red and blue areas indicate whether the odd or even states yield the largest signal and white for which the states are indistinguishable. **c**–**e**, Zoom-ins of QD charge difference with $t_L = t_R = 0.5E_{ABS}$, $\theta = \pi/8$ and $\mu_C = 0.75\Delta_P$ (**c**), $\mu_C = 2.5\Delta_P$ (**d**) and $\mu_C = 0.3\Delta_P$ (**e**). Here various tilts of the $\mu_{LD} = \frac{\Delta - t}{\Delta + t}\mu_{RD}$ line are shown as emphasized by the black arrows. Grey arrows indicate the width of the transitions, set by Δ and t. **f**–**h**, Parity polarization maps for $t_L = t_R = 0.4E_{ABS}$, $\theta = \pi/8$, $T_p = 0.2\Delta_P$, with $\mu_C = 0.75\Delta_P$ (**f**), $\mu_C = 2.5\Delta_P$ (**g**) and $\mu_C = 0.3\Delta_P$ (**h**). These maps match the experimental behaviour observed in Extended Data Fig. 5. **i**, Average parity lifetime $\tau_{avg} = 1/(\Gamma_{e\to o} + \Gamma_{o\to e})$ for same parameters as in panel **f**. **j**, Schematic of the poisoning process, Γ_Δ, which decreases the lifetime in the centre of **i** by means of poisoning to the excited states. The x-axis corresponds to the blue arrow in **i**. Details on the model can be found in Methods section 'Model', with calculations on the quantum capacitance and charge sensing signals in subsection 'Quantum capacitance and charge sensing' and state occupation in subsection 'Occupation'.

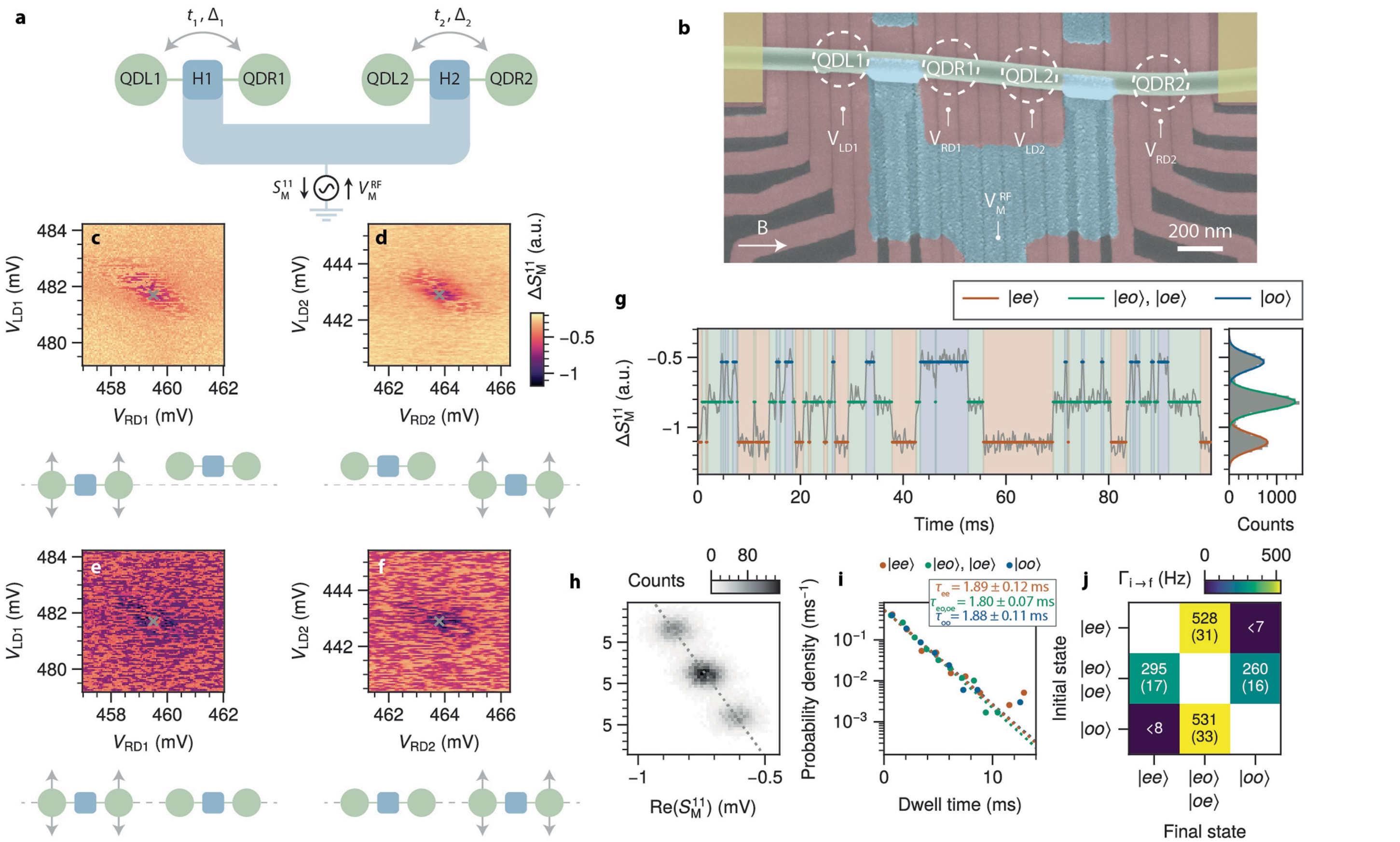

Extended Data Fig. 11 | Quantum capacitance parity readout of two minimal chains in a qubit geometry. a, Schematic of a device with two minimal Kitaev chains coupled to a common superconductor and an off-chip resonator. Each chain contributes a parity-dependent quantum capacitance: $C_Q^{1(2)} \propto 1/\Delta_{1(2)}$ (if the chain is even) and $C_Q^{1(2)} = 0$ (if the chain is odd), in which $\Delta_{1(2)}$ is the CAR coupling of the first (second) chain. The total quantum capacitance for the four possible parity states is $C_Q^{ee} \propto 1/\Delta_1 + 1/\Delta_2$, $C_Q^{eo} \propto 1/\Delta_1$, $C_Q^{oe} \propto 1/\Delta_2$ and $C_Q^{oo} = 0$. If the chains are asymmetric ($\Delta_1 \neq \Delta_2$), four states can be distinguished. On the other hand, if $\Delta_1 \approx \Delta_2$, the two globally odd states cannot be distinguished. Nevertheless, the two even states can always be distinguished both from each other and from the globally odd state[41]. **b**, False-coloured scanning electron micrograph of a device with two chains. The nanowire is depleted between inner dots QDR1 and QDL2 to prevent inter-chain tunnelling. Ohmic contacts (yellow) were added in a second fabrication step. The rightmost QD was shifted by one gate to the right, because the gate closest to the superconductor was too strongly screened to form a suitable tunnel barrier. **c**,**d**, Charge-stability diagram of the left chain while the QDs of the right chain are off resonance (**c**) and vice versa (**d**). In this case, the quantum capacitance readout is sensitive to the parity of only one chain. Parity-switching events appear as telegraph noise in the centre of the charge-stability diagrams, as discussed in Fig. 2. For this measurement and the following ones, the two chains were not fine-tuned to the sweet spot $t = \Delta$. **e**,**f**, Charge-stability diagram of the left chain while the QDs of the right chain are on resonance (**e**) and vice versa (**f**). The telegraph noise in the background corresponds to parity-switching events of the chain whose QDs are not being detuned. At the centre of the charge-stability diagram, all of the QDs are on resonance and more than two states can be detected. **g**, Time trace with the QDs of both chains on resonance, taken at the gate settings marked by grey crosses in **c**–**f**. Three levels are resolved, consistent with $\Delta_1 \approx \Delta_2$, at which the odd states merge. A Gaussian mixture model (see Methods section 'Time traces measurement and analysis') identifies the states, with the central state twice as probable. This result demonstrates single-shot readout in the computational basis |ee⟩, |oo⟩ for a potential PMM qubit, while also enabling detection of leakage into the global odd manifold. A full investigation of parity–qubit operation will be the subject of future work. **h**, Histogram of the complex time trace plotted in **g**. The one-dimensional time trace was obtained by projecting the complex data onto the principal component axis, drawn here with a dotted line. **i**, Distribution of the dwell times for the three identified states. The good match with an exponential model confirms that the switching processes are Poissonian. The average dwell times are comparable with those measured in the single-chain device. **j**, Transition rates and their standard deviation for the three-state switching process. No direct |ee⟩ ↔ |oo⟩ were observed. The corresponding matrix entries are the estimated upper bound (95% confidence level). This confirms the absence of inter-chain tunnelling.